Journal Pre-proof

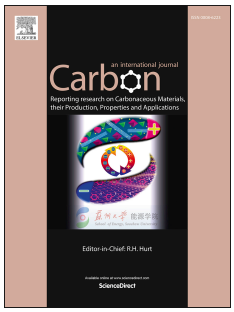

Multi-shell hollow porous carbon nanoparticles with excellent microwave absorption properties

Jiaqi Tao, Jintang Zhou, Zhengjun Yao, Zibao Jiao, Bo Wei, Ruiyang Tan, Zhong Li

PII: S0008-6223(20)31032-0

DOI: https://doi.org/10.1016/j.carbon.2020.10.062

Reference: CARBON 15778

To appear in: *Carbon*

Received Date: 19 August 2020

Revised Date: 12 October 2020

Accepted Date: 13 October 2020

Please cite this article as: J. Tao, J. Zhou, Z. Yao, Z. Jiao, B. Wei, R. Tan, Z. Li, Multi-shell hollow porous carbon nanoparticles with excellent microwave absorption properties, *Carbon*, https://doi.org/10.1016/j.carbon.2020.10.062.

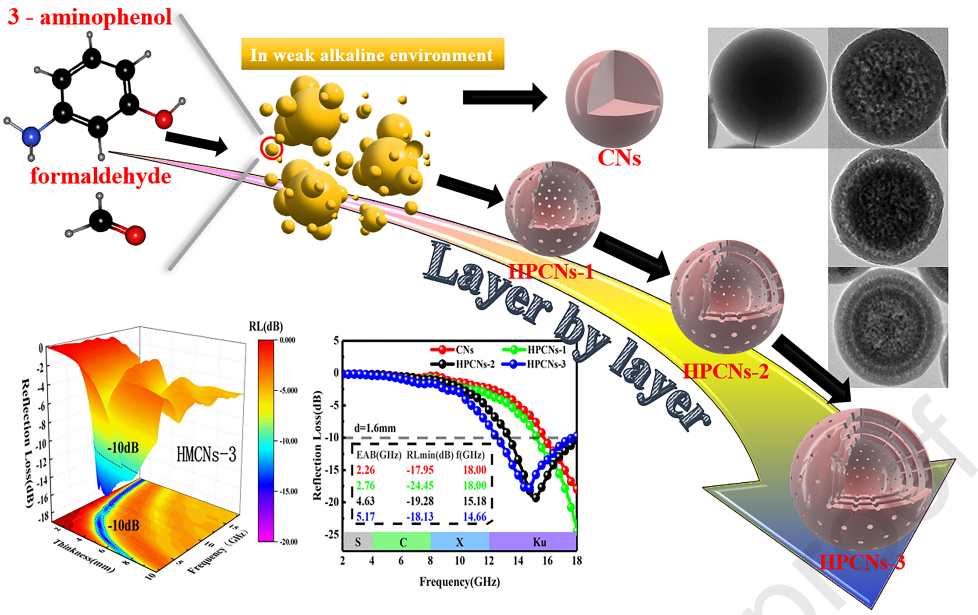

Multi-shell hollow porous carbon nanoparticles with excellent microwave absorption properties

Jiaqi Tao[a,b], Jintang Zhou[a,b,*], Zhengjun Yao[a,b], Zibao Jiao[a,b], Bo Wei[a,b], Ruiyang Tan[a,b], Zhong Li[a,b,**]

[a] College of Materials Science and Technology, Nanjing University of Aeronautics and Astronautics, Nanjing, 211100, Jiangsu, People's Republic of China

[b] Key Laboratory of Material Preparation and Protection for Harsh Environment (Nanjing University of Aeronautics and Astronautics), Ministry of Industry and Information Technology, Nanjing, 211100, Jiangsu, People's Republic of China

[*] Corresponding author. College of Materials Science and Technology, Nanjing University of Aeronautics and Astronautics, Nanjing, 211100, Jiangsu, People's Republic of China.

[**] Corresponding author. College of Materials Science and Technology, Nanjing University of Aeronautics and Astronautics, Nanjing, 211100, Jiangsu, People's Republic of China.

Phone: +8613814115821

E-mail address: imzjt@126.com (J. Zhou), nuaalizhong@163.com (Z. Li).

Abstract：

The micro-morphology design of nanomaterials has always been a hot issue in the field of microwave absorption. In this work, multi-shell structure is made on the basis of hollow structure and porous structure, and the effect of shell number of nanoparticles on microwave absorption properties is studied. Multi-shell hollow porous carbon nanoparticles (HPCNs-m) were prepared by simple liquid phase method combined with layer-by-layer process, and their micro-morphology, chemical structure, electromagnetic properties and microwave absorption properties were studied by a variety of characterization methods. The results show that the multi-shell structure is beneficial to improve the conductivity loss and polarization loss, so as to enhance the microwave absorption properties of the samples. In all samples, the effective absorption bandwidth (EAB) of three-shell hollow porous carbon nanoparticles (HPCNs-3) is 5.17 GHz under the thickness of 1.6 mm, and the best reflection loss (RL) is -18.13 dB at 14.66 GHz. This work expands the study of the effect of the number of shells on microwave absorption properties, and provides a useful reference for the design of microwave absorbers.

Keywords：Hollow; porous; Multi-shell; Layer-by-Layer; Microwave absorption

1. Introduction

In recent years, excessive electromagnetic radiation has caused electromagnetic pollution, which has caused many adverse effects on human health and military applications [1-5]. In order to solve the problem of electromagnetic pollution, people try to use electromagnetic shielding materials or microwave absorbing materials to solve the problem. Electromagnetic shielding materials are easy to cause secondary pollution, while microwave absorbing materials can convert electromagnetic energy into thermal energy. Compared with electromagnetic shielding materials, the latter is obviously more environmentally friendly and effective, so it is widely concerned by the scientific community [6-8]. For absorbing materials, it is necessary not only to pursue large microwave absorption intensity and wide effective absorption bandwidth, but also to take into account the requirements of light weight and thin thickness, which is beneficial to practical application [9, 10]. Carbon based materials, such as carbon nanoparticles [11, 12], carbon nanotubes [13, 14], graphene [15-18], have gradually become the focus in the field of microwave absorption due to their high chemical stability, low density and controllable dielectric properties [19].

The Charming morphology is one of the important reasons why nanomaterials attract scholars. Many new nanostructures, such as hollow structure [20-22], porous structure [23-25], core-shell structure [26, 27], yolk-shell structure [28], often appear in the frontier research. Unique morphology is often accompanied by excellent performance. Xu et al. prepared hollow carbon particles by a template method, and the effective absorption bandwidth of the sample at a thickness of 3.5 mm covered the

entire X-band [29]. Zhou et al. obtained hollow carbon particles with an effective absorption bandwidth of 4.8 GHz at a thickness of 1.9 mm by adjusting the calcination temperature [30]. Not only that, the change of morphology has a direct impact on the properties of nanomaterials. Zhang et al. found that the dielectric constant and impedance matching characteristics can be effectively controlled by adjusting the aperture and shell thickness [31]. Chen et al. enhanced the polarization capability of materials by adjusting the pore volume, thus obtaining excellent absorbent [32]. The research on wave absorption of single shell hollow porous carbon nanoparticles has been very rich [33], but it is a pity that there is no systematic study on the wave-absorbing properties of multi-shell hollow porous carbon nanoparticles [34].

Multi-shell hollow porous structure can be regarded as a composite structure of hollow structure, porous structure and core-shell structure, which has the characteristics of light weight, high specific surface area, high biocompatibility and high transmission efficiency [35]. However, complexity of structures and lack of pervasive synthesis methods make them difficult to prepare. Currently there is no efficient and convenient preparation mode, and the multi-shell can only be obtained by continuous cyclic steps, which makes the experimental period long and requires high precision [36]. Nevertheless, the multi-shell hollow porous structure still has made great achievements in the fields of energy storage, catalysis, sensors, and drug delivery [37, 38]. Even among the thousands of nanostructures used for electromagnetic wave absorption, it is extremely special. The multi-shell hollow

structure not only integrates the characteristics of hollow, porous and core-shell, but also its interface increases with the increase of the number of shells (each shell has internal and external surfaces), which is very conducive to the occurrence of polarization. Besides, in the process of orderly combination of hollow shells of different sizes, its composition (metallic oxides and nonmetal), shape (rod, sphere, polyhedra), shell layer parameters (size, thickness, spacing, porosity of shells) can be flexibly adjusted to obtain the desired electromagnetic characteristics. Thus hopefully obtaining better electromagnetic performance and electromagnetic wave absorption performance than ordinary nanostructures above [39]. Simulation results show that adjusting shell parameters can improve electromagnetic wave absorption efficiency even achieve sequence absorbing effect [40, 41]. It can be inferred that the multi-shell structure with adjustable shell and rich interfaces may have unique advantages in microwave absorption, and research on microwave absorption of multi-shell structures needs to be expanded.

In this work, single-shell hollow porous carbon nanoparticles were prepared by template-free method, and on this basis, the shell was successfully coated by layer-by-layer process, and different shell numbers of hollow porous carbon nanoparticles were obtained. The results show that controlling the number of shells is an effective means to adjust the microwave absorption properties. After characterizing the electromagnetic properties and microwave absorption properties of the samples, it is found that with the increase of the number of shells, the impedance matching of the samples decreases, but the microwave absorption properties are enhanced. On the one

hand, the increase of the number of shells increases the particle size of electromagnetic waves and enhances the reflection of nanoparticles to electromagnetic waves. Although it is not conducive to the incidence of electromagnetic waves, it enhances the loss of incident electromagnetic waves. On the other hand, the introduction of hollow structure, porous structure and multi-shell structure brings more interfaces and defects, which are conducive to interface polarization and dipole polarization, and enhance the attenuation of samples to electromagnetic waves. In addition, nitrogen doping and tight shell of multi-shell structure are beneficial to the transition and movement of electrons, which increases the conductivity loss of the material. In all samples, the three-shell hollow porous carbon nanoparticles (HPCNs-3) have the effective absorption bandwidth of 5.17 GHz and the best reflection loss of -18.13 dB under the thickness of 1.6 mm. This work fills the gap of the effect of the number of shells on the microwave absorption properties of carbon nanoparticles, and provides an idea for the design of high-performance microwave absorbers.

2. Experimental section

2.1 Materials

The chemical reagents in this work and their specifications are shown in Table 1.

Table 1

Reactant properties.

Reactant	Manufacture	Purity, %
3-aminophenol	Nanjing Reagent, China	99.0
Formaldehyde solution	Solution Nanjing Reagent, China	37.0
Ammonia solution	Nanjing Reagent, China	25.0
Ethanol absolute	Sinopharm Chemical ReagentCo., Ltd	99.5
Acetone	Macklin, China	99.7

2.2 Synthesis of carbon nanoparticles (CNs) and Single-shell hollow porous carbon nanoparticles (HPCNs-1)

Phenolic resin nanoparticles were synthesized by the polycondensation reaction of aldehyde and phenol, and the hollow porous structure was obtained after selective cleaning with acetone, and finally the experimental samples were obtained by carbonization at high temperature. Firstly, 0.5 g 3-aminophenol and 0.5 ml ammonia solution was added to the mixed solution of 100 ml deionized water and 50 ml anhydrous ethanol, and magnetically stirred for 5 min. After that, the 0.5 ml formaldehyde solution was added to the mixture drop by drop, and the 30 min was stirred by magnetic force, then poured into 100 ml acetone and left standing for 2 h.

After centrifuging with deionized water for three times and drying overnight in an oven at 60 □, single shell hollow porous nanoparticles (HPNs-1) were obtained in the form of yellowish powder. The HPNs-1 was placed in a tube furnace filled with argon, heated to 800 □ at a heating rate of 3 □/min for 6 h, and cooled at room temperature to obtain single-shell hollow porous carbon nanoparticles (HPCNs-1). The product of high temperature carbonization of the powder obtained without washing with acetone is solid carbon nanoparticles (CNs).

2.3 Synthesis of Multi-shell hollow porous carbon nanoparticles (Take HPCNs-2 as an example)

The multi-layer shell structure was obtained by classical layer-by-layer process [38, 42, 43]. The collected HPNs-1 was placed in a mixed solution containing 0.75 g 3-aminophenol, 0.75 ml ammonia solution, 150 ml deionized water and 75 ml anhydrous ethanol, and ultrasonic dispersion for 30 min. After that, the 0.75 ml formaldehyde solution was added to the mixture drop by drop, and the 30 min was stirred by magnetic force. Then 150 ml of acetone was poured into it and left standing for 2 h. After centrifugation and drying, two-shell hollow porous nanoparticles (HPNs-2) were obtained. HPNs2 was carbonized at high temperature by the same method as above, two-shell hollow porous carbon nanoparticles (HPCNs-2) were obtained. The reactant of HPNs-3 is twice that of HPNs-2.

2.4 Characterization

The morphology and structure of the samples were observed by field emission scanning electron microscope (FE-SEM, JEOL JSM-7001F) and field emission transmission electron microscope (TEM; JEOL JEM-2100). After degassing at 160 □ for 3 hours under vacuum conditions, the N_2 adsorption-desorption isotherm was collected with a high-speed automatic area and pore analyzer (TriStar 3000), and the pore size distribution and specific surface area were calculated. The crystal structure of the sample was characterized by X-ray diffractometer (XRD, Bruker D8 Advance) under the irradiation of Cu K α (λ = 0.15418 nm). At the laser wavelength of 532 nm, the Raman spectrum was obtained by confocal Raman spectrometer (Raman, WITec Alpha300R). The chemical composition of the sample was determined by X-ray photoelectron spectroscopy (XPS) under the irradiation of Al Kα (1486.6 eV). The sample and KBr powder were pressed into thin sheets, and the composition of functional groups was determined by Fourier transform infrared spectroscopy (FT-IR, NICOLETIS-10). The electromagnetic parameters of the samples were obtained by coaxial method. Press 2.5 parts of samples and 7.5 parts of paraffin into a ring shape (outer radius: 7.00 mm; inner radius: 3.04 mm), and measure with a vector network analyzer (VNA, CETC CeYear 3672B).

3. Results and discussion

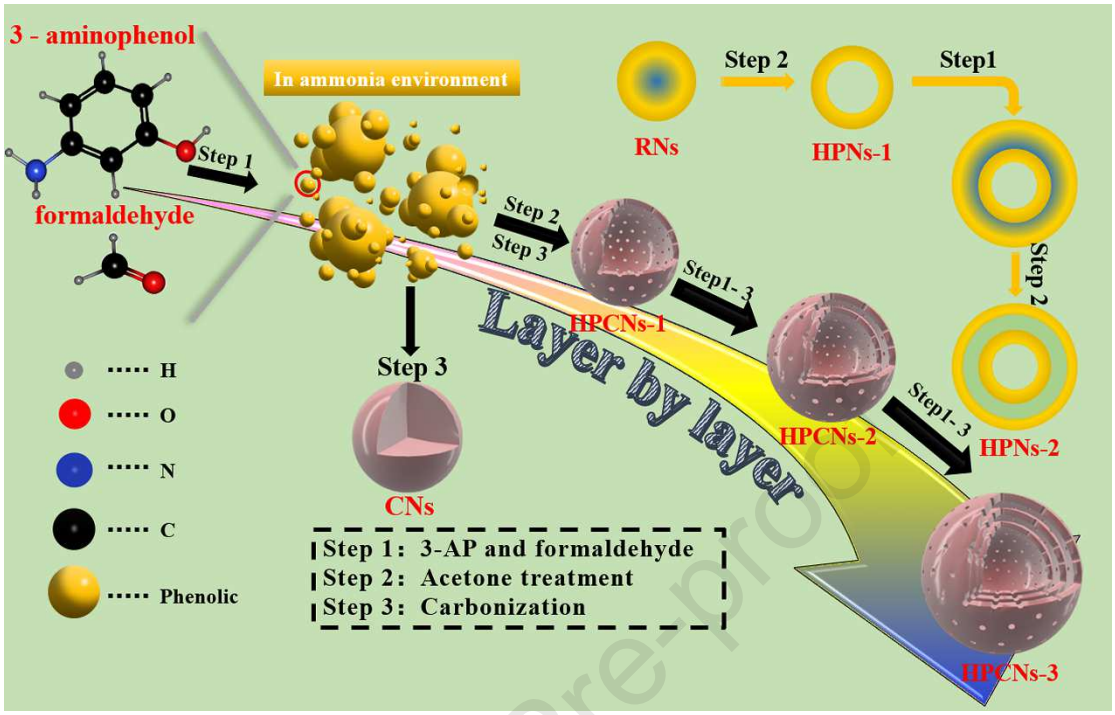

Fig. 1. The schematic diagram of the synthesis process for HPCNs-m.

Multi-shell hollow porous carbon nanoparticles (HPNs-m) were prepared by layer-by-layer process, and then carbonized at high temperature to obtain multi-shell hollow porous carbon nanoparticles (HPCNs-m). The schematic diagram of the synthesis process for sample is shown in Fig. 1. First of all, 3-aminophenol and formaldehyde were Polycondensed in alkaline ($NH_3 \cdot H_2O$) ethanol solution [44, 45], and the solid phenolic resin nanoparticles (RNs) was formed by the reaction of 30 min under the condition of magnetic stirring. In this step of the reaction, because of the time difference between the formation of phenolic resin molecules, the small phenolic molecules generated later will agglomerate on the surface of the phenolic resin generated first and gradually become spherical. Because the outer layer of phenolic resin particles can fully contact with ammonia, the reaction degree of external resin is

higher than that of internal resin. Making use of this property, the hollow structure can be obtained by dissolving the part of phenolic resin particles with low reaction degree with suitable concentration of acetone solution [38]. At the same time, the appropriate ethanol/water ratio is conducive to the construction of porous structure, which is consistent with other studies [31, 32, 46]. After adding acetone and standing for 2 h, then centrifuging with deionized water three times, drying in an oven of 60 □ for one night, the yellowish phenolic resin powder was collected. The phenolic resin powder without acetone treatment and phenolic resin powder with acetone treatment was heated in a tube furnace filled with argon at a rate of 3 □/min to 800 □ and held for 6 h for carbonization, to obtain CNs and HPCNs-1, respectively. The structure of multi-shell is prepared on the basis of single shell, taking HPCNs-2 as an example. When the prepared HPNs-1 was uniformly dispersed in the mixed solution (3 aminophenol, ammonia, ethanol, deionized water) and added drop by drop to the formaldehyde solution, the newly formed phenolic resin particles would still reunite and grow on the surface of the existing phenolic resin particles. Then use the same concentration of acetone solution to dissolve the less reactive part of the second growth phenolic resin, and finally carbonize to obtain HPCNs-2. In theory, more shells can be obtained by using layer-by-layer process as long as the amount of raw materials and acetone is adjusted reasonably. In this experiment, the sample with the most shell is HPCNs-3.

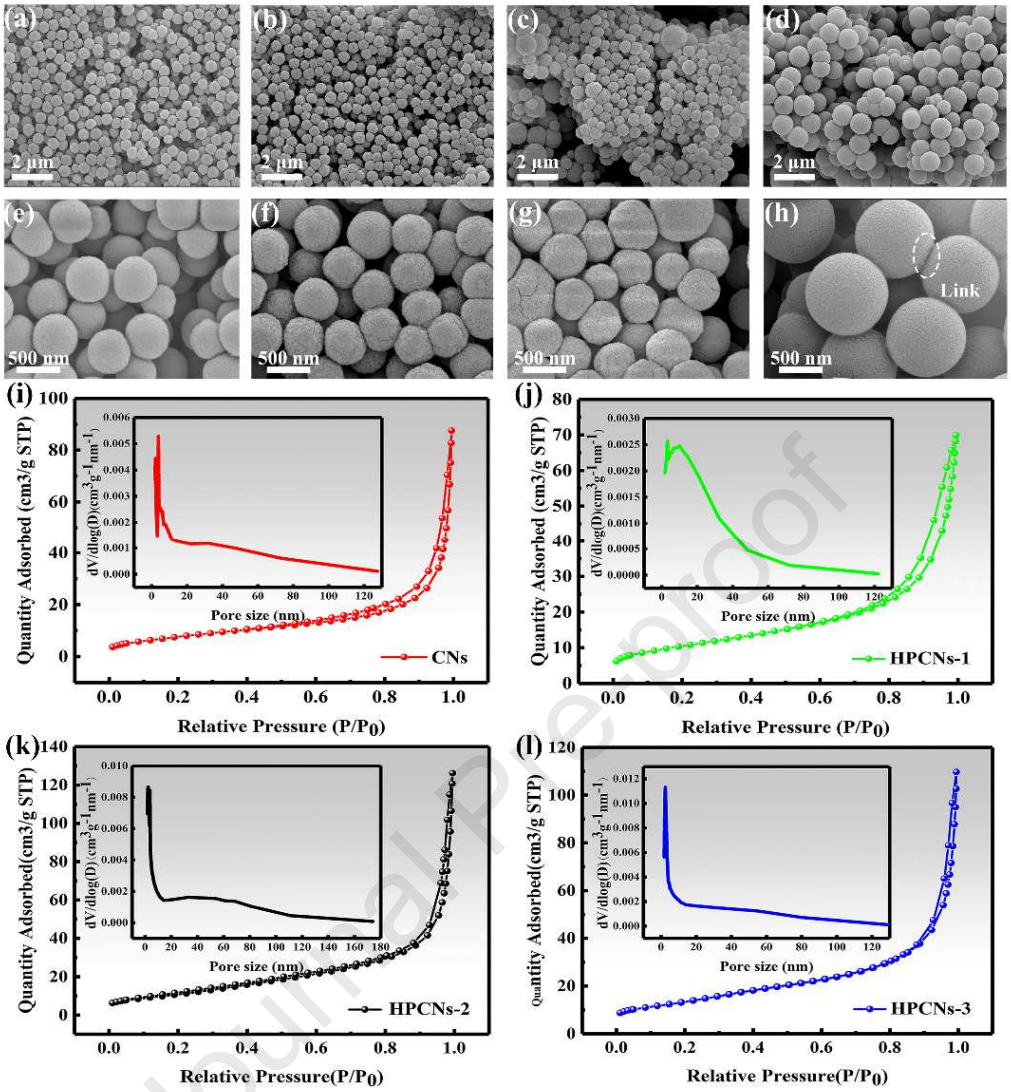

Fig. 2. SEM images of CNs (a, e), HPCNs-1 (b, f), HPCNs-2 (c, g), HPCNs-3 (d, h). Nitrogen adsorption-desorption isotherms and pore size distributions calculated result (i-l).

The surface morphology of the sample can be observed by SEM image, as shown in Fig. 2a-h. At a larger scale, well-formed carbon nanoparticles can be seen. In the process of continuous coating of the shell, the particle size becomes larger, and the average size of CNs and HPCNs-1 is about 550 nm. Larger particles have appeared in the image of HPCNs-2. Finally, the average size of HPCNs-3 is the largest of the four

groups of samples, close to 1 μm. Not only that, the size uniformity of the particles will also be affected by the shell coating, which can be confirmed by the appearance of carbon particles of different sizes in Fig. 2c. On a smaller scale, it can be seen that the surface of the sample shows a rough sense of particles. In addition, in the process of multi-shell preparation, it is inevitable to find multiple nanoparticles sintered together, which is conducive to the conduction of electrons between particles. The N_2 adsorption-desorption isotherm (Fig. 3i-l) of the sample shows a typical IV-type isotherm, indicating that the sample has a porous structure [47]. The pore size distribution of the sample also shows that the material is porous. Whether it is hollow structure, porous structure or multi-shell structure, it can reduce the density of the material and increase the specific surface area of the material (Table S1). Based on the conductive network model and the mechanism of aggregation-induced charge transport, lighter samples can increase the density of the micro-conductive network, thus enhancing the conductivity loss [48-50]. Moreover, these structures can also bring a large number of heterogeneous interfaces and defects, which are conducive to interface polarization and dipole polarization. In addition, it has been reported that holes and depressions can act as dihedral angles to enhance microwave scattering and reflection [51, 52].

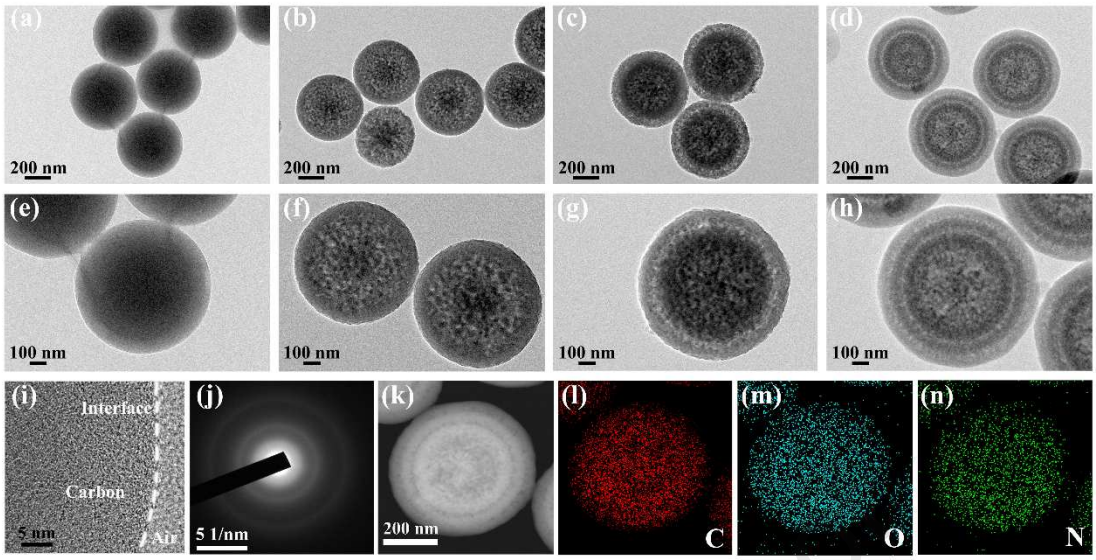

Fig. 3. TEM images of CNs (a, e), HPCNs-1 (b, f), HPCNs-2 (c, g), HPCNs-3 (d, h). HR-TEM image (i), SAED result (j) and Element mapping (k-n) of HPCNs-3.

The internal structure of the sample can be observed through the TEM image of the sample, as shown in Fig. 3a-h. The size of the nanoparticles is consistent with the SEM test results, showing an increasing trend. Except for the solid structure of CNs, obvious cavities can be found in the other three groups of samples. The appearance of thin black lines where the particles are connected is observed in Fig. 3e, which shows that the particles are connected rather than happen to touch. Perhaps the formation of conductive networks has something to do with these thin black lines. Fig. 3f-h also confirms that HPCNs-1, HPCNs-2 and HPCNs-3 correspond to single shell, double shell and three shell, respectively. Interestingly, there are a lot of gaps between layers, which leads to a large number of interfaces. Of course, there are not always gaps between the shell layers. The contact of the inner and outer shells will promote the conduction of electrons inside the particles, forming a tiny conductive network. HPCNs-3 element mapping (Fig. 3k-n) and EDX analysis results (Fig. S1) show that

C (88.39 wt%), O (3.81 wt%) and N (7.8 wt%) are uniformly distributed in the nanoparticles. Lattice fringes were not captured in high resolution TEM (Fig. 3i) and no clear diffraction points were found in SAED (Fig. 3j) which indicated that carbon was amorphous. However, it is necessary to note that TEM and electron diffraction results in local regions cannot prove the non-existence of the graphite in whole samples because some nano-crystalline graphite is hard to be detected [53].

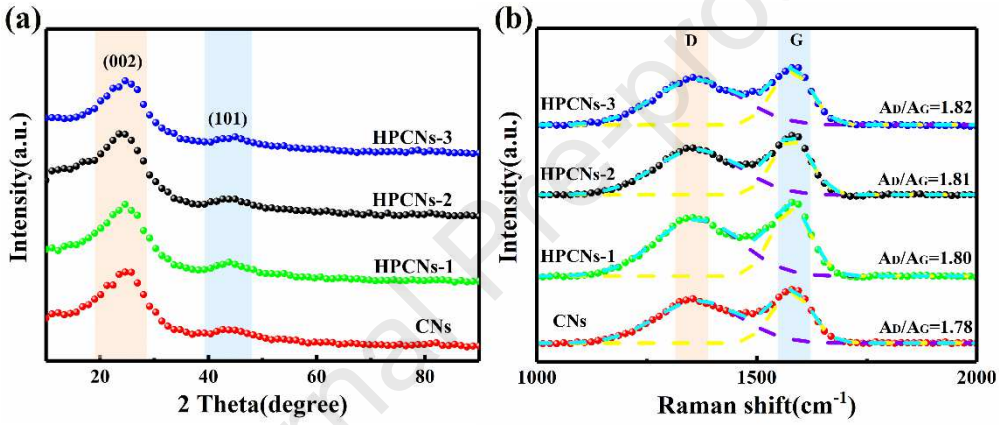

Fig. 4. XRD patterns (a) and Raman spectra (b) of samples.

In the XRD spectra (Fig. 4a), the wide peak at 25° represents the (0 0 2) crystal face of amorphous carbon, and the weak bulge at 44.1° originates from the (1 0 1) crystal face of graphite which imply that graphite may exist in the sample. The Raman spectra of all samples are shown by Fig. 4b, and two obvious characteristic peaks of carbon are observed at the positions of 1340 cm^{-1} and 1590 cm^{-1}, which are defined as D band and G band, respectively. In general, D-band is caused by defects and disorder and the wide D band in the figure indicates that the crystal structure of the material is in great disorder and there are many defects. The G band is caused by sp^2 hybrid carbon, which represents the order of graphite and provides strong evidence for the

presence of graphite in the sample. The area ratio (A_D/A_G) of D-band to G-band reflects the degree of graphitization of materials [54, 55]. According to the integral areas values of D and G peaks (Table S2), the A_D/A_G values of CNs, HPCNs-1, HPCNs-2 and HPCNs-3 are 1.78, 1.80, 1.81 and 1.82 respectively. The ratio shows a slight growth trend, which may be due to the fact that the multi-shell structure can bring more defects. At the same time, the large A_D/A_G may be explained by the following reasons. A large number of oxygen atoms in phenolic resin are removed in the process of high temperature carbonization, leaving many vacancy defects. The unremoved oxygen atoms exist in the form of asymmetric oxygen-containing groups, which disturbs the sp^2 state of graphite, resulting in amorphous and low graphitization of the samples [48]. Combined with Tem, SAED, XRD and Raman, it was obvious that samples were mainly amorphous and accompanied by localized graphitization phenomena. The existence of amorphous carbon is not conducive to the movement of electrons and may have a negative effect on the conductivity loss of materials. However, relatively, a large number of defects in amorphous carbon can be used as the polarization center of the dipole, which can produce dipole turning polarization under the action of electromagnetic field, which is beneficial to enhance the polarization loss [31]. In addition, the defects in the graphite layer, like those in carbon nanotubes, may produce additional states near the Fermi level, causing the electromagnetic wave energy in the microwave band to be absorbed through the adjacent states on the Fermi level [56-58]. It is can be speculated that the samples in this experiment may have great polarization loss ability.

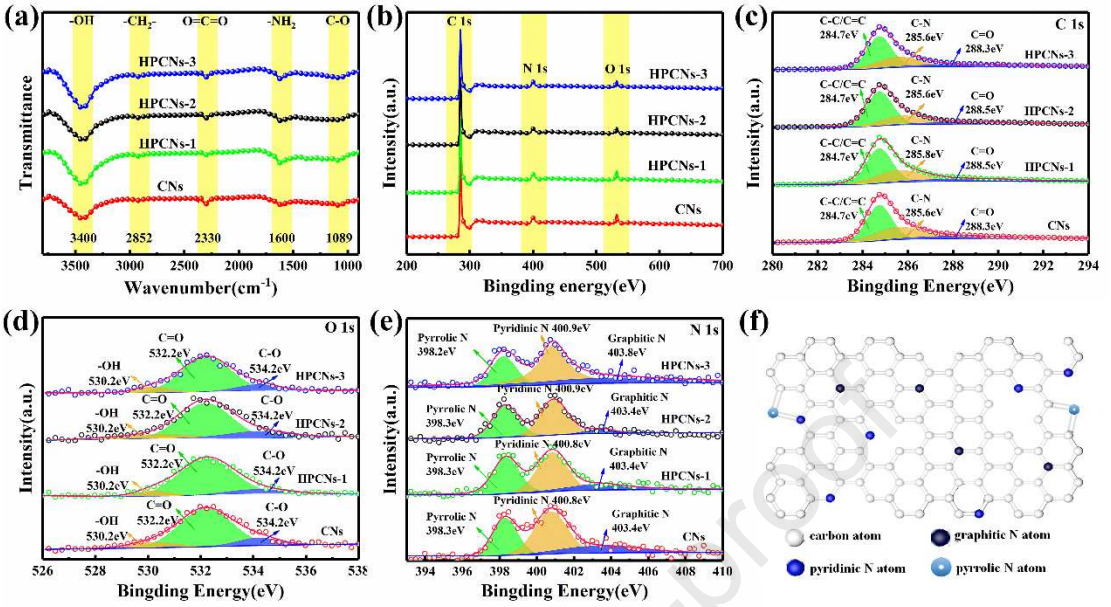

Fig. 5. FT-IR spectrum (a) and XPS spectrum (b) of samples, high resolution C 1s XPS spectrum of samples (c), high resolution N 1s XPS spectrum of samples (d), high resolution O 1s XPS spectrum of samples (e), schematic structure of N (f).

In order to understand the chemical structure of the material, we carried out infrared tests, and the results are as shown by Fig. 5a. The broad peak at 3400cm^{-1} is thought to be the stretching vibration of -OH, which may come from the sample or from the moisture in the air. The weak peak at 2852 cm^{-1} comes from -CH_2-, which is the product of the reaction of phenols with aldehydes [23]. The peaks at 1600 cm^{-1} and 1089 cm^{-1} come from -NH_2 and C-O, respectively. These residual polar groups are usually regarded as the polarization center of the dipole, which can induce the dipole to turn polarization, which is beneficial to enhance the polarization loss, thus improving the microwave absorption capacity of the material [31]. The chemical

elements and surface electronic states of the samples were further studied by XPS spectra, as shown by Fig. 5b-e. According to the XPS total spectrum (Fig. 5b) of the samples, the characteristic peaks of C 1s, N 1s and O 1s were detected in the four samples, indicating that the samples were composed of C, N and O elements, which was consistent with the previous test results. It is worth mentioning that because of the difference in electronegativity between C, N and O, these atoms can also be used as polarization centers of dipoles, thus enhancing the polarization loss [16]. The high resolution C 1s XPS spectrum of samples (Fig. 5c) shows that there are three characteristic peaks at 284.7 eV, ~ 285.6 eV and ~ 288.5 eV, corresponding to C-C/C=C, C=N, C=O [49, 59]. The high resolution O 1s XPS spectrum of samples (Fig. 5d) shows that three characteristic peaks can be observed at 530.2 eV, 532.2 eV and 534.2 eV, corresponding to -OH, C=O, C-O [24]. The high resolution N 1s XPS spectrum of samples (Fig. 5e) shows that the nitrogen in the sample is composed of three parts, and the three characteristic peaks at ~ 398.2 eV, 400.8 eV, 403.4 eV correspond to pyridine nitrogen, pyrrole nitrogen and graphite nitrogen, respectively [60]. Various forms of nitrogen doping in partially graphitized carbon conductive networks (Fig. 5f) promote the movement of electrons and contribute to the conductivity loss of materials [9, 16]. At the same time, N atom doping will produce some positive and negative charges in the adjacent C and N atoms, which can be used as polarization centers, thus increasing the polarization loss [29]. Therefore, nitrogen doping is beneficial to improve the electromagnetic wave loss of the material.

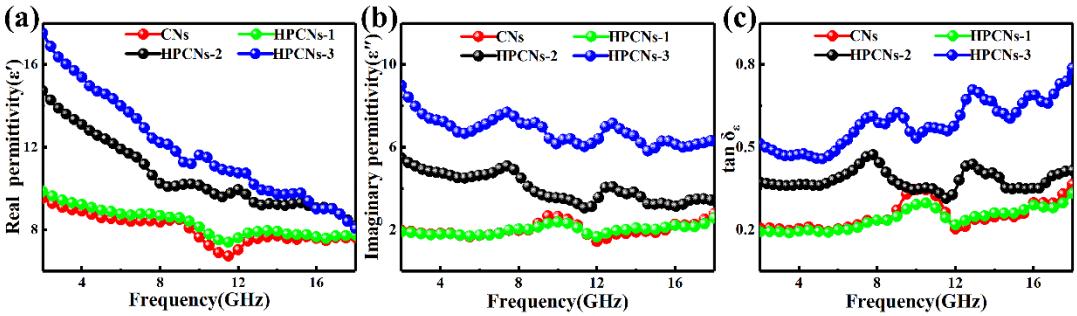

Fig. 6. The real (ε′) and imaginary (ε′′) of complex permittivity (a, b), and tan δ_ε (c) versus frequency.

In order to explore the influence of the combination of multi-shell structure on microwave absorption properties, it is necessary to study the changes of electromagnetic parameters. According to the transmission line theory [61], there is a close relationship between complex permittivity (ε_r) and magnetic permeability (μ_r) and microwave absorption properties. The permeability and tan δ_μ of the sample are shown in Fig. S2 and Fig. S3. All samples have similar permeability which fluctuates slightly with the change of frequency. This fluctuation may be related to the magnetic moment in disordered carbon materials. The H atoms attached to the zigzag edge of nano-graphite and the vacancy defects in disordered carbon interact with impurities (H or N atoms) to produce magnetic moment, which leads to the change of magnetic permeability [62, 63]. However, the values of μ' and μ" are close to 1 and 0, respectively, indicating the negligible magnetic loss. Thus, the complex permittivity of the sample deserves more attention.

The real part (ε') of the complex permittivity represents the storage capacity of the material to electric energy or the degree of response to electromagnetic field, and

the imaginary part (ε") represents the power loss ability of the material to electric energy [15]. The electromagnetic parameters of all samples in the range of 2-18 GHz were measured at room temperature, and the Debye relaxation model was used to help understand. ε_r, ε', ε" can be represented respectively by Eq. (1-3) [31]:

$$\varepsilon_r = \varepsilon_\infty + \frac{\varepsilon_s - \varepsilon_\infty}{1 + j2\pi f\tau} = \varepsilon' - j\varepsilon'' \quad (1)$$

$$\varepsilon' = \varepsilon_\infty + \frac{\varepsilon_s - \varepsilon_\infty}{1 + (2\pi f)^2\tau^2} \quad (2)$$

$$\varepsilon'' = \frac{2\pi f\tau(\varepsilon_s - \varepsilon_\infty)}{1 + (2\pi f)^2\tau^2} \quad (3)$$

where ε_∞ is the optical dielectric constant, ε_s is the static dielectric constant, τ is the relaxation time, f is the frequency. The relationship between ε′, ε″, tan δ_ε and f is shown in Fig. 6. Compared with the other three groups of samples, the complex permittivity of HPCNs-3 is significantly increased. The variation of complex permittivity of pure carbon materials is usually related to chemical structure and microstructure [64]. XRD (Fig. 4a) proved that all samples were amorphous carbon, Raman (Fig. 4b), FT-IR and XPS (Fig. 5) proved that they have similar bonding states (graphitization degree) and chemical groups. Perhaps the remarkable changes in microstructure of this experimental system had more direct influence on complex permittivity of materials. In the multi shell structure, each shell is rich in many interfaces (inner surface, outer surface and pore interface). With the increase of the number of shells, the increase of interface becomes more and more obvious, because the outer shell size is always larger than the inner shell size. The hanging bond on the interface of the multi-shell structure can bind more space charge, thus increasing the

storage of electric energy and increasing the ε′ [21]. Usually, the dielectric loss of materials is divided into polarization loss and conductance loss. In the form of polarization loss, because electron displacement polarization and ion displacement polarization occur very quickly, they do not have a visible effect on the complex permittivity, so only interface polarization and dipole polarization are considered in microwave band [20]. According to the Maxwell-Wagner model, the aggregation of space charge at heterogeneous interfaces (paraffin-carbon, air-carbon and crystalline-amorphous) leads to interfacial polarization which will dissipate electrical energy [65-68]. The oxygen vacancy defects and residual polar functional groups (hydroxyl group, carbonyl group, etc.) in the shell can be regarded as the polarization center of the dipole to generate dipole polarization and consume electromagnetic wave [51]. When the accumulated space charge is too much, the weak current will be generated, which will form different degrees of conductive network between multiple particles or in the shell of a single multi-shell particle, so that the electromagnetic energy will be transformed into thermal energy [41]. HPCNs-3 with three shells has the most interfaces, which is conducive to the formation of multi polarization and the enhancement of space charge conduction, so its ε″ is larger than other samples. The largest electrical loss tangent (tan δ_ε=ε″/ε′) of HPCNs-3 (Fig. 6c) also indicates the strongest dielectric loss capability [69]. The change of tan δ_ε with frequency (from 0.5 at 2 GHz to 0.8 at 18 GHz) is more obvious than that of the other three groups of samples, which indicates the excellent high frequency response. The phenomenon about ε′ decrease with increasing frequency within the range of 2-18 GHz is attributed

to the hysteresis of dielectric polarization caused by the change of electromagnetic field, which is called dielectric dispersion [6]. In addition, compared with HPCNs-3 and HPCNs-2, the dielectric parameters of HPCNs-1 are closer to CNS. The change from solid to single-layer hollow structure only brings the increase of inner surface, while the increase of each shell in multi-shell structure can bring inner surface, outer surface and pore interface. In short, the multi shell structure can increase the storage and loss of electromagnetic energy, and the gain is much stronger than the single shell structure, which is expected to enhance the microwave absorption performance.

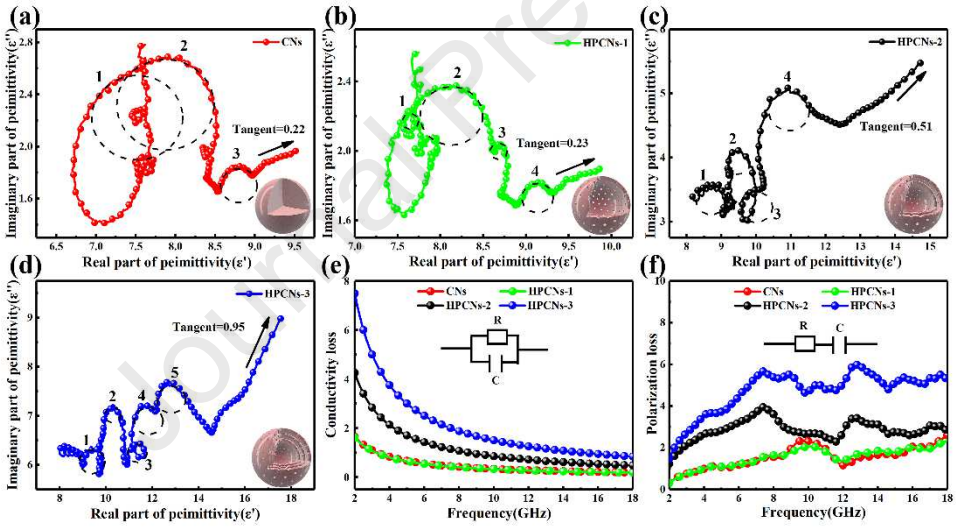

Fig. 7. Cole-Cole semicircles of CNs (a), HPCNs-1 (b), HPCNs-2 (c), and HPCNs-3 (d). Conductivity loss (e) and Polarization loss curve (f).

In order to further clarify the origin of the microwave absorption properties of the samples, we need to focus on the relaxation behavior. The relaxation process is usually related to the Cole-Cole semicircle. On the basis of Eq. (2) and Eq. (3), the relationship between ε' and ε'' can be expressed by Eq. (4) [2]：

$$(\varepsilon' - \frac{\varepsilon_\infty + \varepsilon_s}{2})^2 + (\varepsilon'')^2 = (\frac{\varepsilon_s - \varepsilon_\infty}{2})^2 \quad (4)$$

The relation curve of ε', ε'' is called Cole-Cole semicircle, and each semicircle represents the Debye relaxation process related to interfacial polarization or dipole polarization. It can be seen from the Fig. 7a-d that all the four samples have multiple relaxation processes, and the values of ε'' and ε' corresponding to the upper vertex of the dotted circle almost correspond to the frequency of the formant in Fig. 6c. The matrix of amorphous carbon contains a large number of defects and polar groups, which provides conditions for dipole polarization, so non-hollow CNs can also have three relaxation processes. By comparison, it is known that HPCNs-3 has at least five relaxation processes, which are the most in all samples. Since the effect of the multi-shell structure on the graphitization degree of the matrix (only a slight increase) is not enough to bring about a huge change in dipole polarization, the difference in the polarization ability of the samples is more suitable to be attributed to the increase of interfacial polarization. There is a small tail at the end of all Cole-Cole curves that tends to be linear. The greater the slope of the line segment, the greater the conductivity loss of the material, which is beneficial to improve the wave-absorbing properties. In the analysis of dielectric loss, the contribution of conductance loss and polarization loss is an interesting problem. According to Eq. (5), the nonlinear equation is used to fit the original electromagnetic parameters of the sample [15]：

$$\varepsilon'' = \varepsilon_p'' + \varepsilon_c'' = (\varepsilon_s - \varepsilon_\infty)\frac{2\pi f \tau}{1 + (2\pi f)^2 \tau^2} + \frac{\sigma}{2\pi f \varepsilon_0} \quad (5)$$

where ε_p'' is the contribution of polarization loss, ε_c'' is the contribution of conductance loss, σ is the conductivity and ε_0 is the vacuum permittivity. The fitting

results can be divided into conductance loss curve (Fig. 7e) and polarization loss curve (Fig. 7f). The equivalent circuit of conductance loss is equivalent to the parallel circuit of resistance and capacitor, while the equivalent circuit of polarization loss is equivalent to the series circuit of resistance and capacitor [68, 70]. In Fig. 7e, the conductance loss curves of all samples show the same trend, that is, the conductance loss decreases with the increase of frequency. There is also a positive correlation between the number of shells and the conductivity loss, and the conductivity loss of HPCNs-3 is significantly higher than that of the other three groups of samples. On the one hand, it may be because the outer shell of a single particle collapses after annealing and forms a conductive network with the inner shell. On the other hand, it may be because the particle size of HPCNs-3 is large, so it is easier for particles to contact each other to form a conductive network. In addition, the doping of nitrogen is beneficial to the migration and transition of electrons [71]. In Fig. 7f, the polarization loss increases with the increase of frequency. And at the same frequency, the more the number of shells, the greater the polarization loss. It is worth noting that the frequency corresponding to the peak of the polarization loss curve is very close to that of the formant of the ε" curve (Fig. 6b), which verifies the location of the polarization relaxation. The fitting results of conductance loss and polarization loss and Cole-Cole diagram well confirm the following two conclusions: the multi shell structure can enhance the conductivity loss and polarization loss, and the enhancement of polarization ability is reflected in the increase of interface polarization; the effect of polarization loss is greater than that of conductivity loss (mainly conductivity loss in

2-4 GHz and polarization loss in 4-18 GHz).

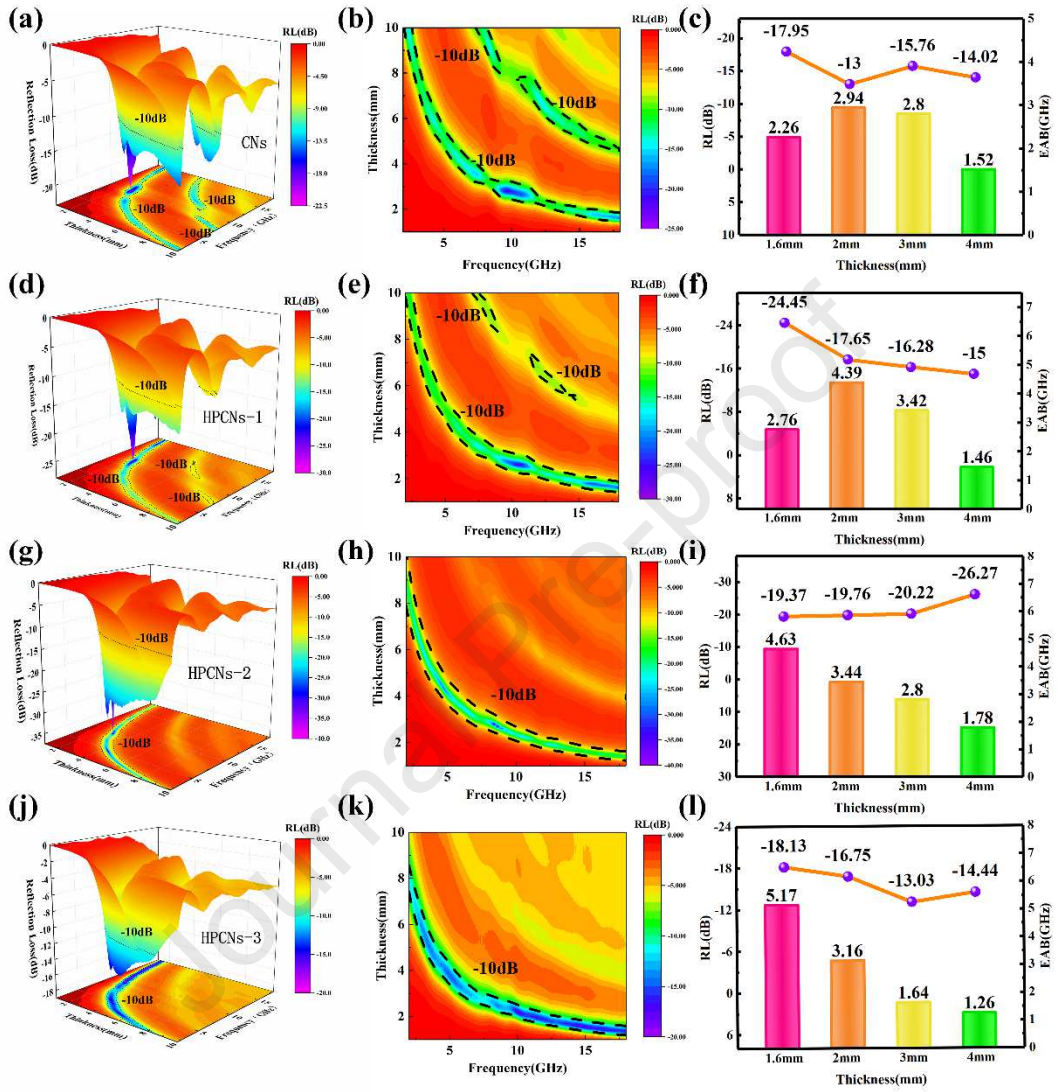

Fig. 8. 3D RL map, 2D RL contour map, RL value and EAB value between thickness range of 1.6–4.0 mm of CNs (a, b, c), HPCNs-1 (d, e, f), HPCNs-2 (g, h, i) and HPCNs-3 (j, k, l).

In order to evaluate the microwave absorption efficiency of the sample, the reflection loss RL is derived from the transmission line theoretical model, such as Eq. (6) and Eq. (7) [72]：

$$RL(\mathrm{dB}) = 20\log\left|(Z_{in}-1)/(Z_{in}+1)\right| \quad (6)$$

$$Z_{in} = \sqrt{\frac{\mu_r}{\varepsilon_r}}\tanh\left[\mathrm{j}(2\pi fd/c)\sqrt{\mu_r\varepsilon_r}\right] \quad (7)$$

where Z_{in} is the normalized input impedance of the material, f is the frequency of microwave, d is the thickness of the material, and c is the propagation velocity of electromagnetic wave in vacuum. In practical applications, the part where the RL value is less than -10 dB is considered to be the effective absorption bandwidth (EAB), because it already represents that 90% of the electromagnetic waves are absorbed [73, 74]. The three-dimensional and two-dimensional reflection loss maps of all samples and the RL and EAB values under the corresponding thickness are shown in Fig. 8. The parts of the three-dimensional and two-dimensional graphs that effectively absorb bandwidth have been marked with dotted lines. The reflection loss of each group of samples showed a similar rule, and the values of EAB and RL gradually moved to low frequency with the increase of sample thickness. In order to meet the requirement of "thin" microwave absorber in practical application, the change law of microwave absorption property below 4 mm thickness of the sample was analyzed. When the thickness of CNs increases, the RL value increases, and the minimum value is -17.95 dB at 1.6 mm, while the EAB increases at first and then decreases, and reaches the widest 2.94 GHz at 2 mm (Fig. 8a-c). The best RL value of HPCNs-1 under 1.6 mm thickness is -24.45 dB, and its EAB increases at first and then decreases with the increase of thickness, reaching the widest 4.39 GHz at 2 mm (Fig. 8d-f). When the thickness of HPCNs-2 increases, the values of EAB and RL decrease continuously, the widest EAB is 4.63 GHz at 1.6 mm, and the best RL value is -26.27 dB at 4 mm

(Fig. 8g-i). Finally, it is surprising that HPCNs-3 achieves the widest EAB and the best RL values under the thickness of 1.6 mm, which are 5.17 GHz and -18.13 dB respectively (Fig. 8j-l). There is no doubt that the microwave absorbing property of HPCNs-3 is the best among the four groups of samples, thanks to the largest number of carbon shells.

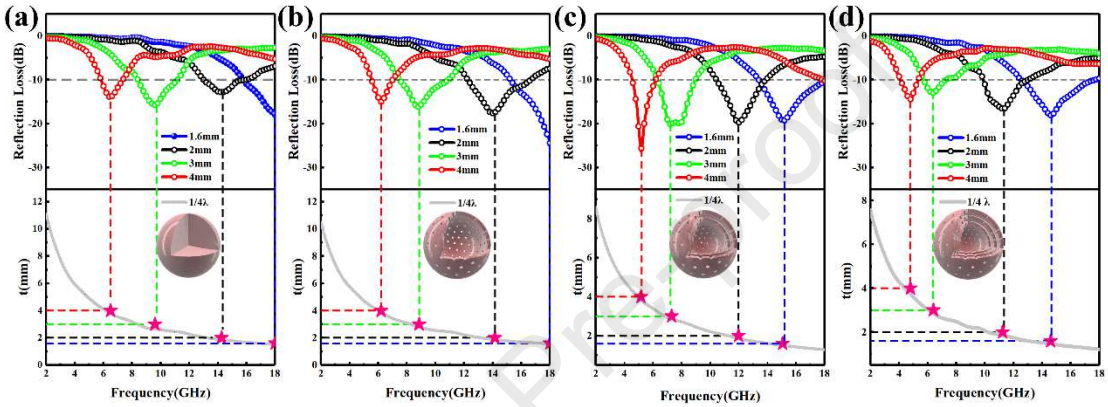

Fig. 9. Reflection loss (RL)-frequency curves, relationship between simulated thickness and the peak frequency for CNs (a), HPCNs-1 (b), HPCNs-2 (c), HPCNs-3 (d).

The EAB and peak frequency found in Fig. 8 gradually shift to low frequency with the increase of sample thickness, which conforms to the law of 1/4 wavelength matching model (1/4λ) [26]. In order to further study the absorbing properties, it is necessary to clarify the relationship between matching frequency (f_m) and matching thickness (t_m), expressed by Eq. (8):

$$t_m = n\lambda/4 = nc/(4f_m\sqrt{|\mu_r||\varepsilon_r|}) \quad n=(1,3,5...) \quad (8)$$

where t_m is the matching thickness, λ is the wavelength of microwave, c is the velocity of light, f_m is the matching frequency. Obviously, the intersection of the

vertical line of the frequency corresponding to the RL peak and the vertical line of the thickness of the absorbing sample ideally falls on the 1/4λ curve (Fig. 9). The cause of this phenomenon is related to the cancellation of electromagnetic waves. Electromagnetic waves are reflected twice at the material-air interface and the material-metal (metal substrate in the test instrument) interface. The reflected electromagnetic wave has an odd multiple of half the wavelength, so interference cancellation occurs, which weakens the electromagnetic wave. In addition, the relationship between t_m and ε_r is well illustrated by Eq. (8). Because HPCNs-2 and HPCNs-3 have larger ε_r values, they can achieve the best electromagnetic wave absorption performance under the thickness of 1.6 mm.

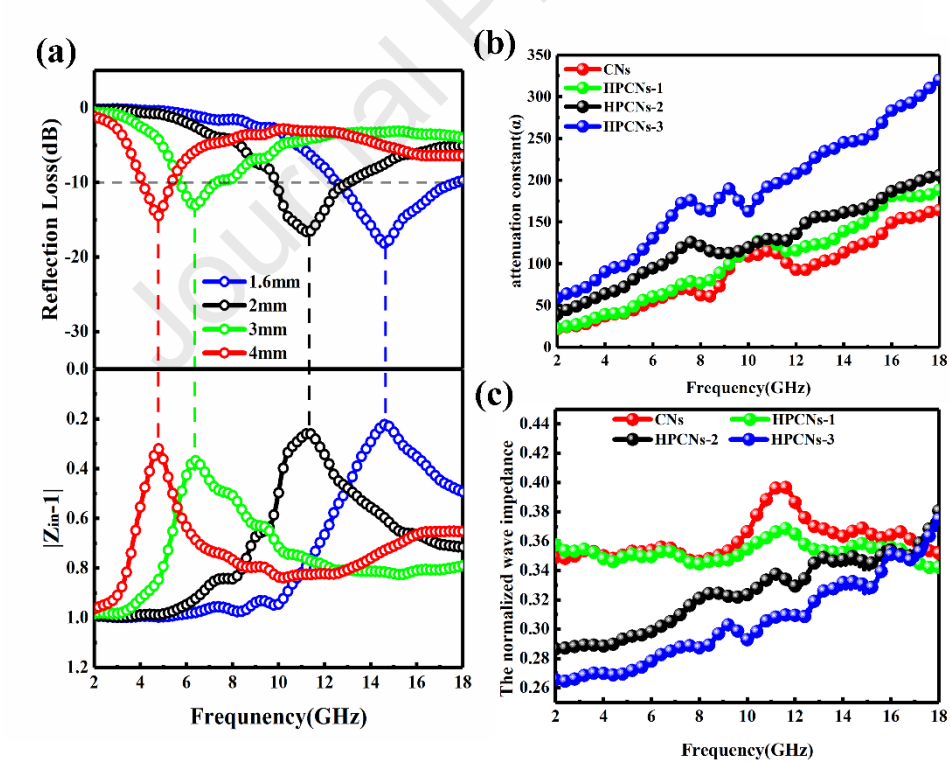

Fig. 10. The calculated $|Z_{in}-1|$ values represent for the impendence matching of HPCNs-3 (a). the normalized wave impedance (b) and attenuation constant (c) of all samples.

The ability of absorbing materials to allow the incidence of electromagnetic waves is called impedance matching, which is expressed by Eq. (6-7). As shown in Fig. 10a, the closer $|Z_{in}-1|$ is to zero, the stronger the RL feature is [75]. However, compared with the other samples (Fig. S4), the $|Z_{in}-1|$ value of HPCNs-3 has no advantage. This is because the difference between permittivity and permeability is too large, which has an adverse effect on impedance matching [76, 77].

When the electromagnetic wave enters the interior of the sample, the attenuation degree of the electromagnetic wave of the sample can be characterized by the attenuation factor α, which is expressed by Eq. (9) [51, 54]:

$$\alpha = \frac{\sqrt{2}\pi f}{c}\sqrt{(\mu''\varepsilon'' - \mu'\varepsilon') + \sqrt{(\mu''\varepsilon'' - \mu'\varepsilon')^2 + (\mu'\varepsilon'' + \mu''\varepsilon')^2}} \quad (9)$$

Fig. 10b is the relationship between attenuation factor and frequency of each sample. At the same frequency, the α value of the material is positively correlated with the number of shells. The more the number of shells, the stronger the attenuation of electromagnetic waves. In addition, the α values of all samples showed an upward trend. Among them, the rising rate of HPCNs-3 is the highest, with a value of 59 at 2 GHz and 320 at 18 GHz, which may be due to the fact that the multi-shell structure can increase the high-frequency response of the material itself. Combining the results of impedance matching and attenuation factor, the excellent microwave absorption energy absorption of the sample in Ku band can be explained, as shown by Fig. S5. The excellent absorbing performance of HPCNs-3 is mainly due to its outstanding electromagnetic wave attenuation ability.

Usually in practical applications, it is necessary to consider the first wave reflection of the electromagnetic wave, which can be expressed by the normalized wave impedance Z (Eq. (10)), so as to give full play to the attenuation performance of the material [78].

$$Z = \left| \sqrt{\frac{\mu_r}{\varepsilon_r}} \right| \quad (10)$$

As shown in Fig. 10c, although HPCNs-3 has the best absorbing performance, its Z value is the lowest as a whole, indicating that its surface reflection is on the high side. Table 2 shows some recently reported studies on hollow carbon nanoparticles. The microwave absorption properties of HPCNs-3 are comparable to those of these excellent absorbers, indicating that multi-shell hollow porous carbon nanoparticles have great potential. In the future, we will devote to exploring multi-shell nano-absorbers with better impedance matching and better microwave absorption.

Table 2 .

Microwave absorption properties of several wave absorbers reported recently.

Sample	Optimal R_L value (dB)	Absorption Bandwidth (GHz)	Thickness (mm)	Ref.
HGs@PAC-5	/	4.2	3.5	[29]
HCN-6	-50.8	4.8	1.9	[30]
PCHMs-650 ℃	-28	5.28	2.6	[31]

PCHMs	/	~ 4.1	3.1	[46]
core-shell Co@C nanotubes	-48	5.2	1.8	[71]
Porous magnetic carbon	-52	5	1.7	[79]
Porous Ni/C microspheres	-28.4	~ 4.5	1.8	[80]
Amorphous PC/Fe3O4@Fe	-49.6	5.2	2	[81]
Nanoporous carbon	/	4.8	1.8	[82]
HPCNs-3	-18.13	5.17	1.6	This work

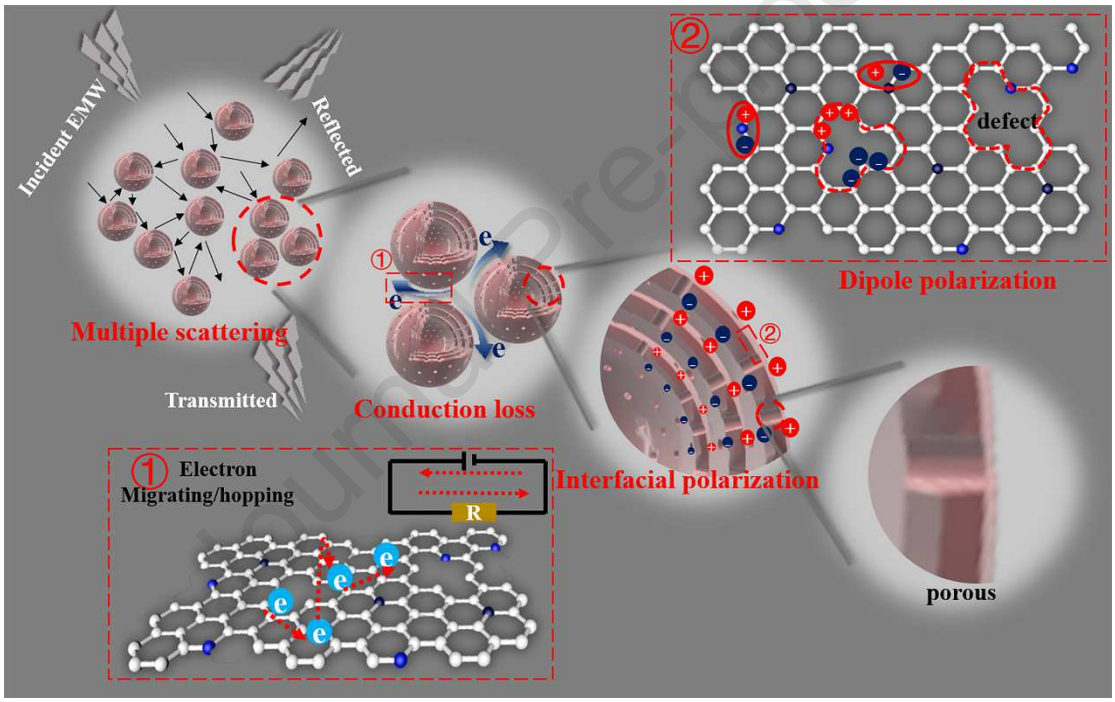

Fig. 11. Schematic diagram of the microwave absorption mechanism of the sample.

Fig. 11 is a schematic diagram of the microwave absorption mechanism of the sample. First of all, the phenomena of reflection, scattering and transmission will occur when the electromagnetic wave is in contact with the surface of absorbing agent particles. In this process, the electromagnetic energy is transformed and dissipated

[83]. Second, the contact between the surfaces of multiple nanoparticles and the contact between different shells of a single nanoparticle due to collapse and other reasons will promote the formation of conductive network and enhance the conductivity loss [71]. In addition, the doping of N is beneficial to the migration and transition of electrons, and also promotes the conductivity loss [29]. Third, the residual polar groups and rich defects in amorphous carbon will become the polarization center of the dipole. The dipole rotates and collides constantly under the action of the electromagnetic field, which converts the electromagnetic energy into thermal energy [29, 47]. Fourth, multi-shell hollow porous structure can bring more micro-interface and enhance the effect of interface polarization [60]. In summary, under the synergistic action of various loss mechanisms, the excellent absorbing performance of HPCNs-3 is obtained.

4. Conclusion

In a word, multi-shell hollow porous carbon nanoparticles were prepared by layer-by-layer process. The results show that the multi-shell hollow porous structure can improve the conductivity loss and polarization loss of the material to electromagnetic wave. At the same time, the multi-shell structure increases the particle size of the material, thus strengthening the reflection of electromagnetic waves. HPCNs-3 has good microwave absorption performance in the case of poor impedance matching, which is due to its excellent electromagnetic wave attenuation ability. When the thickness of HPCNs-3 is 1.6 mm, EAB is 5.17 GHz and RL is

-18.13 dB. More importantly, this work fills the deficiency in the study of the effect of multi-shell structure on microwave absorption properties, and has a certain reference value for the structural design of high-performance microwave absorbers.

Declaration of competing interest

The authors declare that they have no known competing financial interests or personal relationships that could have appeared to influence the work reported in this paper.

Acknowledgments

This work is supported by the National Natural Science Foundation of China (51672129 and 52002337), Open Fund of Key Laboratory of Materials Preparation and Protection for Harsh Environment (Nanjing University of Aeronautics and Astronautics), Ministry of Industry and Information Technology (56XCA19013-05).

References:

[1] Y. Zuo, Z. Yao, H. Lin, J. Zhou, P. Liu, W. Chen, C. Shen, Coralliform $Li_{0.35}Zn_{0.3}Fe_{2.35}O_4$/polyaniline nanocomposites: Facile synthesis and enhanced microwave absorption properties, J. Alloy. Compd. 746 (2018) 496-502.

[2] B. Wei, J. Zhou, Z. Yao, A.A. Haidry, X. Guo, H. Lin, K. Qian, W. Chen, The effect of Ag nanoparticles content on dielectric and microwave absorption properties of β-SiC, Ceram. Int. 46 (2020) 5788-5798.

[3] J. Zhou, R. Tan, Z. Yao, H. Lin, Z. Li, Preparation of $CoFe_2O_4$ hollow spheres with carbon sphere templates and their wave absorption performance, Mater. Chem. Phys. 244 (2020) 122697.

[4] Z. Gao, Z. Jia, K. Wang, X. Liu, L. Bi, G. Wu, Simultaneous enhancement of recoverable energy density and efficiency of lead-free relaxor-ferroelectric BNT-based ceramics, Chem. Eng. J. 402 (2020) 125951.

[5] X. Chen, W. Wang, T. Shi, G. Wu, Y. Lu, One pot green synthesis and EM wave absorption performance of MoS_2@nitrogen doped carbon hybrid decorated with ultrasmall cobalt ferrite nanoparticles, Carbon 163 (2020) 202-212.

[6] A. Ling, G. Tan, Q. Man, Y. Lou, S. Chen, X. Gu, R. Li, J. Pan, X. Liu, Broadband microwave absorbing materials based on MWCNTs' electromagnetic wave filtering effect, Compos. B. Eng. 171 (2019) 214-221.

[7] X. Zhang, F. Yan, S. Zhang, H. Yuan, C. Zhu, X. Zhang, Y. Chen, Hollow N‑Doped Carbon Polyhedron Containing CoNi Alloy Nanoparticles Embedded within Few-Layer N‑Doped Graphene as High-Performance Electromagnetic Wave Absorbing Material, Acs Appl. Mater. Inter. 10 (2018) 24920-24929.

[8] S. Biswas, G.P. Kar, S. Bose, Attenuating microwave radiation by absorption through controlled nanoparticle localization in PC/PVDF blends, Phys. Chem. Chem. Phys. 17 (2015) 27698-27712.

[9] Z. Sun, Z. Yan, K. Yue, A. Li, L. Qian, Novel high-performance electromagnetic absorber based on Nitrogen/Boron co-doped reduced graphene oxide, Compos. B. Eng. 196 (2020) 108132.

[10] T. Hou, Z. Jia, A. Feng, Z. Zhou, X. Liu, H. Lv, G. Wu, Hierarchical composite of biomass derived magnetic carbon framework and phytic acid doped polyanilne with prominent electromagnetic wave absorption capacity, J. Mater. Sci. Technol. (2020) https://doi.org/10.1016/j.jmst.2020.06.046.

[11] B. Han, W. Chu, X. Han, P. Xu, D. Liu, L. Cui, Y. Wang, H. Zhao, Y. Du, Dual functions of glucose induced composition-controllable Co/C microspheres as high-performance microwave absorbing materials, Carbon 168 (2020) 404-414.

[12] B. Li, C. Wang, W. Wang, M. Yu, R. Gao, Y. Chen, X. Yan, Electromagnetic wave absorption properties of composites with micro-sized magnetic particles dispersed in amorphous carbon, J. Magn. Magn. Mater. 365 (2014) 40-44.

[13] G. Song, S. Luo, J. Zhang, M. Zhang, G. Qiu, A. Meng, Y. Lin, Z. Li, Template-free one-step synthesis of the multi-layer carbon or stacked graphene sheets coessentially coating N-doped graphene tubes and their field emission and photoluminescence properties, J. Alloy. Compd. 829 (2020) 154411.

[14] X. Xiao, W. Zhu, Z. Tan, W. Tian, Y. Guo, H. Wang, J. Fu, X. Jian, Ultra-small Co/CNTs nanohybrid from metal organic framework with highly efficient microwave absorption, Compos. B. Eng. 152 (2018) 316-323.

[15] P. Liu, Z. Yao, J. Zhou, Z. Yang, L.B. Kong, Small magnetic Co-doped NiZn ferrite/graphene nanocomposites and their dual-region microwave absorption performance, J. Mater. Chem. C 4 (2016)

9738-9749.

[16] Q. Li, X. Tian, W. Yang, L. Hou, Y. Li, B. Jiang, X. Wang, Y. Li, Fabrication of porous graphene-like carbon nanosheets with rich doped-nitrogen for high-performance electromagnetic microwave absorption, Appl. Surf. Sci. 530 (2020) 147298.

[17] D. Shun, X. Zhang, X. Li, J. Chen, P. Hu, J. Han, SiC whiskers-reduced graphene oxide composites decorated with MnO nanoparticles for tunable microwave absorption, Chem. Eng. J. 392 (2020).

[18] H. Zhang, Z. Jia, A. Feng, Z. Zhou, L. Chen, C. Zhang, X. Liu, G. Wu, In situ deposition of pitaya-like Fe_3O_4@C magnetic microspheres on reduced graphene oxide nanosheets for electromagnetic wave absorber, Compos. B. Eng. 199 (2020) 108261.

[19] Z. Wang, P. Zhao, P. Li, S. Li, L. Liao, Y. Luo, Z. Peng, D. He, Y. Cheng, Hierarchical cerium oxide anchored multi-walled carbon nanotube hybrid with synergistic effect for microwave attenuation, Compos. B. Eng. 167 (2019).

[20] B. Wei, J. Zhou, Z. Yao, A.A. Haidry, K. Qian, H. Lin, X. Guo, W. Chen, Excellent microwave absorption property of nano-Ni coated hollow silicon carbide core-shell spheres, Appl. Surf. Sci. 508 (2020) 145261.

[21] J. Zhou, B. Wei, Z. Yao, H. Lin, R. Tan, W. Chen, X. Guo, Preparation of hollow SiC spheres with biological template and research on its wave absorption properties, J. Alloy. Compd. 819 (2020) 153021.

[22] J. Xie, L. Liu, J. Xia, Y. Zhang, M. Li, Y. Ouyang, S. Nie, X. Wang, Template-Free Synthesis of Sb_2S_3 Hollow Microspheres as Anode Materials for Lithium-Ion and Sodium-Ion Batteries, Nanomicro Lett 10 (2018) 12.

[23] J. Lu, C. Jiao, Z. Majeed, H. Jiang, Magnesium and Nitrogen Co-Doped Mesoporous Carbon with Enhanced Microporosity for CO2 Adsorption, Nanomaterials 8 (2018) 275.

[24] H. Zhang, Z. Jia, A. Feng, Z. Zhou, C. Zhang, K. Wang, N. Liu, G. Wu, Enhanced microwave absorption performance of sulfur-doped hollow carbon microspheres with mesoporous shell as a broadband absorber, Compos. Commun. 19 (2020) 42-50.

[25] X. Zhou, Z. Jia, A. Feng, K. Wang, X. Liu, L. Chen, H. Cao, G. Wu, Dependency of tunable electromagnetic wave absorption performance on morphology-controlled 3D porous carbon fabricated by biomass, Compos. Commun. 21 (2020) 100404.

[26] A. Sheng, Y. Yang, D. Yan, K. Dai, H. Duan, G. Zhao, Y. Liu, Z. Li, Self-assembled reduced graphene oxide/nickel nanofibers with hierarchical core-shell structure for enhanced electromagnetic wave absorption, Carbon 167 (2020) 530-540.

[27] S. Zhang, Z. Qi, Y. Zhao, Q. Jiao, X. Ni, Y. Wang, Y. Chang, C. Ding, Core/shell structured composites of hollow spherical $CoFe_2O_4$ and CNTs as absorbing materials, J. Alloy. Compd. 694 (2017) 309-312.

[28] X. Liu, L. Wang, Y. Ma, Y. Qiu, Q. Xie, Y. Chen, D. Peng, Facile synthesis and microwave absorption properties of yolk-shell ZnO-Ni-C/RGO composite materials, Chem. Eng. J. 333 (2018) 92-100.

[29] H. Xu, X. Yin, M. Zhu, M. Li, H. Zhang, H. Wei, L. Zhang, L. Cheng, Constructing hollow graphene nano-spheres confined in porous amorphous carbon particles for achieving full X band microwave absorption, Carbon 142 (2019) 346-353.

[30] C. Zhou, S. Geng, X. Xu, T. Wang, L. Zhang, X. Tian, F. Yang, H. Yang, Y. Li, Lightweight hollow carbon nanospheres with tunable sizes towards enhancement in microwave absorption, Carbon

108 (2016) 234-241.

[31] H. Zhang, B. Wang, A. Feng, N. Zhang, Z. Jia, Z. Huang, X. Liu, G. Wu, Mesoporous carbon hollow microspheres with tunable pore size and shell thickness as efficient electromagnetic wave absorbers, Compos. B. Eng. 167 (2019) 690-699.

[32] J. Chen, X. Liang, W. Liu, W. Gu, B. Zhang, G. Ji, Mesoporous carbon hollow spheres as a light weight microwave absorbing material showing modulating dielectric loss, Dalton Trans. 48 (2019) 10145-10150.

[33] G. Shen, Y. Xu, B. Liu, P. Du, Y. Li, J. Zhu, D. Zhang, Enhanced microwave absorption properties of N-doped ordered mesoporous carbon plated with metal Co, J. Alloy. Compd. 680 (2016) 553-559.

[34] Y. Qiu, Y. Lin, H. Yang, L. Wang, M. Wang, B. Wen, Hollow Ni/C microspheres derived from Ni-metal organic framework for electromagnetic wave absorption, Chem. Eng. J. 383 (2020) 123207.

[35] Y. Wei, N. Yang, K. Huang, J. Wan, F. You, R. Yu, S. Feng, D. Wang, Steering Hollow Multishelled Structures in Photocatalysis: Optimizing Surface and Mass Transport, Adv. Mater. (2020) 2002556.

[36] W. Wang, Y. Zhao, Y. Zhang, J. Wang, G. Cui, M. Li, Z. Bakenov, X. Wang, Defect-Rich Multishelled Fe-Doped Co_3O_4 Hollow Microspheres with Multiple Spatial Confinements to Facilitate Catalytic Conversion of Polysulfides for High-Performance Li–S Batteries, Acs Appl. Mater. Inter. 12 (2020) 12763-12773.

[37] D. Mao, J. Wan, J. Wang, D. Wang, Sequential Templating Approach: A Groundbreaking Strategy to Create Hollow Multishelled Structures, Adv. Mater. 31 (2018) 1802874.

[38] D. Bin, Z. Chi, Y. Li, K. Zhang, X. Yang, Y. Sun, J. Piao, A. Cao, L. Wan, Controlling the Compositional Chemistry in Single Nanoparticles for Functional Hollow Carbon Nanospheres, J. Am. Chem. Soc. 139 (2017) 13492-13498.

[39] J. Qi, X. Lai, J. Wang, H. Tang, H. Ren, Y. Yang, Q. Jin, L. Zhang, R. Yu, G. Ma, Z. Su, H. Zhao, D. Wang, Multi-shelled hollow micro-/nanostructures, Chem. Soc. Rev. 44 (2015) 6749-6773.

[40] J. Wang, J. Wan, D. Wang, Hollow Multishelled Structures for Promising Applications: Understanding the Structure–Performance Correlation, Accounts Chem. Res. 52 (2019) 2169-2178.

[41] R. Pang, X. Hu, S. Zhou, C. Sun, J. Yan, X. Sun, S. Xiao, P. Chen, Preparation of multi-shelled conductive polymer hollow microspheres by using Fe_3O_4 hollow spheres as sacrificial templates, Chem. Commun. 50 (2014) 12493-12496.

[42] S. Yoon, W.M. Choi, H. Baik, H. Shin, I. Song, M. Kwon, J.J. Bae, H. Kim, Y.H. Lee, J. Choi, Synthesis of Multilayer Graphene Balls by Carbon Segregation from Nickel Nanoparticles, Acs Nano 6 (2012) 6803-6811.

[43] D. Mao, J. Wan, J. Wang, D. Wang, Sequential Templating Approach: A Groundbreaking Strategy to Create Hollow Multishelled Structures, Adv. Mater. 31 (2018) 1802874.

[44] Y. Niu, X. Li, W. Dong, C. Zhang, K. Zhao, F. Wang, H. Wang, Synthesis of N-doped carbon with embedded Fe/Fe_3C particles for microwave absorption, J. Mater. Sci. 55 (2020) 11970-11983.

[45] T. Yang, J. Liu, R. Zhou, Z. Chen, H. Xu, S.Z. Qiao, M.J. Monteiro, N-doped mesoporous carbon spheres as the oxygen reduction reaction catalysts, J. Mater. Chem. A 2 (2014) 18139-18146.

[46] H. Xu, X. Yin, Z. Li, C. Liu, Z. Wang, M. Li, L. Zhang, L. Cheng, Tunable dielectric properties of mesoporous carbon hollow microspheres via textural properties, Nanotechnology 29 (2018) 184003.

[47] T. Huang, Z. Wu, Q. Yu, D. Tan, L. Li, Preparation of hierarchically porous carbon/magnetic particle composites with broad microwave absorption bandwidth, Chem. Eng. J. 359 (2019) 69-78.

[48] L. Quan, F. Qin, D. Estevez, H. Wang, H. Peng, Magnetic graphene for microwave absorbing application: Towards the lightest graphene-based absorber, Carbon 125 (2017) 630-639.

[49] H. Yuan, F. Yan, C. Li, C. Zhu, X. Zhang, Y. Chen, Nickel Nanoparticle Encapsulated in Few-Layer Nitrogen-Doped Graphene Supported by Nitrogen-Doped Graphite Sheets as a High-Performance Electromagnetic Wave Absorbing Material, Acs Appl. Mater. Inter. 10 (2017) 1399-1407.

[50] M. Lu, W. Cao, H. Shi, X. Fang, J. Yang, Z. Hou, H. Jin, W. Wang, J. Yuan, M. Cao, Multi-wall carbon nanotubes decorated with ZnO nanocrystals: mild solution-process synthesis and highly efficient microwave absorption properties at elevated temperature, J. Mater. Chem. A 2 (2014) 10540.

[51] H. Xu, X. Yin, X. Fan, Z. Tang, Z. Hou, M. Li, X. Li, L. Zhang, L. Cheng, Constructing a tunable heterogeneous interface in bimetallic metal-organic frameworks derived porous carbon for excellent microwave absorption performance, Carbon 148 (2019) 421-429.

[52] Z. Wu, K. Tian, T. Huang, W. Hu, F. Xie, J. Wang, M. Su, L. Li, Hierarchically Porous Carbons Derived from Biomasses with Excellent Microwave Absorption Performance, Acs Appl. Mater. Inter. 10 (2018) 11108-11115.

[53] Y. Du, W. Liu, R. Qiang, Y. Wang, X. Han, J. Ma, P. Xu, Shell Thickness-Dependent Microwave Absorption of Core–Shell Fe_3O_4@C Composites, Acs Appl. Mater. Inter. 6 (2014) 12997-13006.

[54] Y. Cheng, Z. Li, Y. Li, S. Dai, G. Ji, H. Zhao, J. Cao, Y. Du, Rationally regulating complex dielectric parameters of mesoporous carbon hollow spheres to carry out efficient microwave absorption, Carbon 127 (2018) 643-652.

[55] M. Shi, D. Bao, S. Li, B. Wulan, J. Yan, Q. Jiang, Anchoring PdCu Amorphous Nanocluster on Graphene for Electrochemical Reduction of N_2 to NH_3 under Ambient Conditions in Aqueous Solution, Adv. Energy Mater. 8 (2018) 1800124.

[56] X. Xie, Y. Pang, H. Kikuchi, T. Liu, The synergistic effects of carbon coating and micropore structure on the microwave absorption properties of Co/CoO nanoparticles., Phys. Chem. Chem. Phys. 18 (2016).

[57] X. Liu, B. Li, D. Geng, W. Cui, F. Yang, Z. Xie, D. Kang, Z. Zhang, (Fe, Ni)/C nanocapsules for electromagnetic-wave-absorber in the whole Ku-band, Carbon 47 (2009) 470-474.

[58] J.Charlier, Defects in Carbon Nanotubes, Accounts Chem. Res. 35 (2002) 1063-1069.

[59] P. Song, H. Qiu, L. Wang, X. Liu, Y. Zhang, J. Zhang, J. Kong, J. Gu, Honeycomb structural rGO-MXene/epoxy nanocomposites for superior electromagnetic interference shielding performance, SM&T 24 (2020) e00153.

[60] P. Liu, S. Gao, Y. Wang, Y. Huang, W. He, W. Huang, J. Luo, Carbon nanocages with N-doped carbon inner shell and Co/N-doped carbon outer shell as electromagnetic wave absorption materials, Chem. Eng. J. 381 (2020) 122653.

[61] Y. Zuo, X. Su, X. Li, Z. Yao, T. Yu, J. Zhou, J. Li, J. Lu, J. Ding, Multimaterial 3D-printing of graphene/$Li_{0.35}Zn_{0.3}Fe_{2.35}O_4$ and graphene/carbonyl iron composites with superior microwave absorption properties and adjustable bandwidth, Carbon 167 (2020) 62-74.

[62] O. Yazyev, Magnetism in disordered graphene and irradiated graphite, Phys. Rev. Lett. 101 (2008) 037203.

[63] S. Ma, J. Xia, V. Srikanth, X. Sun, T. Staedler, X. Jiang, F. Yang, Z. Zhang, Magnetism of amorphous carbon nanofibers, Appl. Phys. Lett. 95 (2009) 263105.

[64] H. Xu, X. Yin, M. Zhu, M. Han, Z. Hou, X. Li, L. Zhang, L. Cheng, Carbon Hollow Microspheres with a Designable Mesoporous Shell for High-Performance Electromagnetic Wave Absorption, Acs

Appl. Mater. Inter. 9 (2017) 6332-6341.

[65] M. Qiao, X. Lei, Y. Ma, L. Tian, X. He, K. Su, Q. Zhang, Application of yolk-shell Fe_3O_4@N-doped carbon nanochains as highly effective microwave-absorption material, Nano Research 11 (2018) 1500-1519.

[66] J. Wang, J. Yang, J. Yang, H. Zhang, Design of a novel carbon nanotube and metal-organic framework interpenetrated structure with enhanced microwave absorption properties, Nanotechnology 31 (2020) 394002.

[67] B. Zhao, X. Guo, W. Zhao, J. Deng, G. Shao, B. Fan, Z. Bai, R. Zhang, Yolk–Shell Ni@SnO_2 Composites with a Designable Interspace To Improve the Electromagnetic Wave Absorption Properties, Acs Appl. Mater. Inter. 8 (2016) 28917-28925.

[68] D. Kuang, L. Hou, S. Wang, H. Luo, L. Deng, J.L. Mead, H. Huang, M. Song, Large-scale synthesis and outstanding microwave absorption properties of carbon nanotubes coated by extremely small FeCo-C core-shell nanoparticles, Carbon 153 (2019) 52-61.

[69] Y. Sun, J. Xu, W. Qiao, X. Xu, W. Zhang, K. Zhang, X. Zhang, X. Chen, W. Zhong, Y. Du, Constructing Two-, Zero-, and One-Dimensional Integrated Nanostructures: an Effective Strategy for High Microwave Absorption Performance, Acs Appl. Mater. Inter. 8 (2016) 31878-31886.

[70] H. Luo, S. Zeng, Y. Tian, H. Zhang, S. Peng, Mechanism of microwave dielectric response in carbon nanofibers enabled BCN composites, J. Mater. Sci. 27 (2016) 10435-10441.

[71] H. Zhao, Y. Cheng, Z. Zhang, J. Yu, J. Zheng, M. Zhou, L. Zhou, B. Zhang, G. Ji, Rational design of core-shell Co@C nanotubes towards lightweight and high-efficiency microwave absorption, Compos. B. Eng. 196 (2020) 108119.

[72] Z. Yang, H. Lv, R. Wu, Rational construction of graphene oxide with MOF-derived porous NiFe@C nanocubes for high-performance microwave attenuation, Nano Res. 9 (2016) 3671-3682.

[73] H. Lv, Y. Guo, Y. Zhao, H. Zhang, B. Zhang, G. Ji, Z.J. Xu, Achieving tunable electromagnetic absorber via graphene/carbon sphere composites, Carbon 110 (2016) 130-137.

[74] G. Wu, Y. Cheng, Z. Yang, Z. Jia, H. Wu, L. Yang, H. Li, P. Guo, H. Lv, Design of carbon sphere/magnetic quantum dots with tunable phase compositions and boost dielectric loss behavior, Chem. Eng. J. 333 (2018) 519-528.

[75] J. Liu, Y. Duan, L. Song, X. Zhang, Constructing sandwich-like polyaniline/graphene oxide composites with tunable conjugation length toward enhanced microwave absorption, Org. Electron. 63 (2018) 175-183.

[76] H. Wang, Y. Dai, W. Gong, D. Geng, S. Ma, D. Li, W. Liu, Z. Zhang, Broadband microwave absorption of CoNi@C nanocapsules enhanced by dual dielectric relaxation and multiple magnetic resonances, Appl. Phys. Lett. 102 (2013) 223113.

[77] A. Hua, Y. Li, D. Pan, J. Luan, Y. Wang, J. He, S. Tang, D. Geng, S. Ma, W. Liu, Z. Zhang, Enhanced wideband microwave absorption of hollow carbon nanowires derived from a template of Al_4C_3@C nanowires, Carbon 161 (2020) 252-258.

[78] H. Lv, G. Ji, X. Liang, H. Zhang, Y. Du, A novel rod-like MnO_2@Fe loading on graphene giving excellent electromagnetic absorption properties, J. Mater. Chem. C 3 (2015) 5056-5064.

[79] J. Fang, Y. Shang, Z. Chen, W. Wei, Y. Hu, X. Yue, Z. Jiang, Rice husk-based hierarchically porous carbon and magnetic particles composites for highly efficient electromagnetic wave attenuation, J. Mater. Chem. C 5 (2017) 4695-4705.

[80] S. Qiu, H. Lyu, J. Liu, Y. Liu, N. Wu, W. Liu, Facile Synthesis of Porous Nickel/Carbon Composite Microspheres with Enhanced Electromagnetic Wave Absorption by Magnetic and

Dielectric Losses, Acs Appl. Mater. Inter. 8 (2016) 20258-20266.

[81] H. Wang, F. Meng, J. Li, T. Li, Z. Chen, H. Luo, Z. Zhou, Carbonized Design of Hierarchical Porous Carbon/Fe_3O_4@Fe Derived from Loofah Sponge to Achieve Tunable High-Performance Microwave Absorption, Acs Sustain. Chem. Eng. 6 (2018) 11801-11810.

[82] H. Zhao, Y. Cheng, H. Lv, B. Zhang, G. Ji, Y. Du, Achieving Sustainable Ultralight Electromagnetic Absorber from Flour by Turning Surface Morphology of Nanoporous Carbon, Acs Sustain. Chem. Eng. 6 (2018) 15850-15857.

[83] K. Yuan, R. Che, Q. Cao, Z. Sun, Q. Yue, Y. Deng, Designed Fabrication and Characterization of Three-Dimensionally Ordered Arrays of Core–Shell Magnetic Mesoporous Carbon Microspheres, Acs Appl. Mater. Inter. 7 (2015) 5312-5319.

Table 1

Reactant properties

Reactant	Manufacture	Purity, %
3-aminophenol	Nanjing Reagent, China	99.0
Formaldehyde solution	Solution Nanjing Reagent, China	37.0
Ammonia solution	Nanjing Reagent, China	25.0
Ethanol absolute	Sinopharm Chemical ReagentCo., Ltd	99.5
Acetone	Macklin, China	99.7

Table 2 .

Microwave absorption properties of several wave absorbers reported recently.

Sample	Optimal R_L value (dB)	Absorption Bandwidth (GHz)	Thickness (mm)	Ref.
HGs@PAC-5	/	4.2	3.5	[29]
HCN-6	-50.8	4.8	1.9	[30]
PCHMs-650 ℃	-28	5.28	2.6	[31]
PCHMs	/	~ 4.1	3.1	[46]
core-shell Co@C nanotubes	-48	5.2	1.8	[71]
Porous magnetic carbon	-52	5	1.7	[79]
Porous Ni/C microspheres	-28.4	~ 4.5	1.8	[80]
Amorphous PC/Fe3O4@Fe	-49.6	5.2	2	[81]
Nanoporous carbon	/	4.8	1.8	[82]
HPCNs-3	-18.13	5.17	1.6	This work

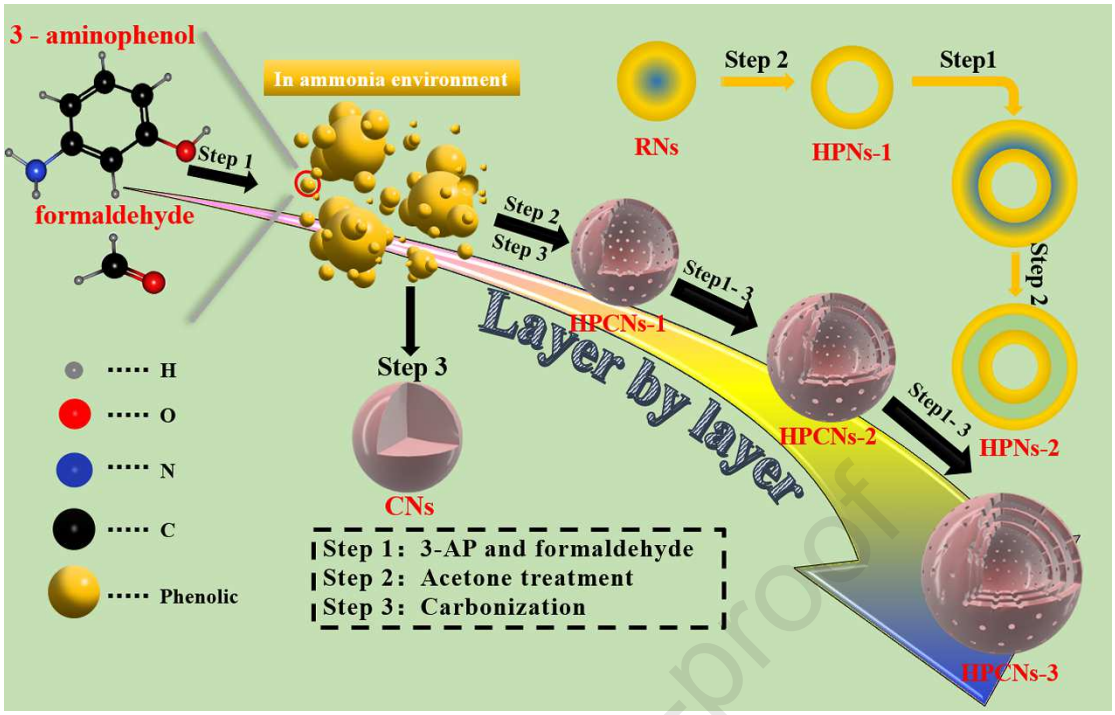

Fig. 1. The schematic diagram of the synthesis process for HPCNs-m.

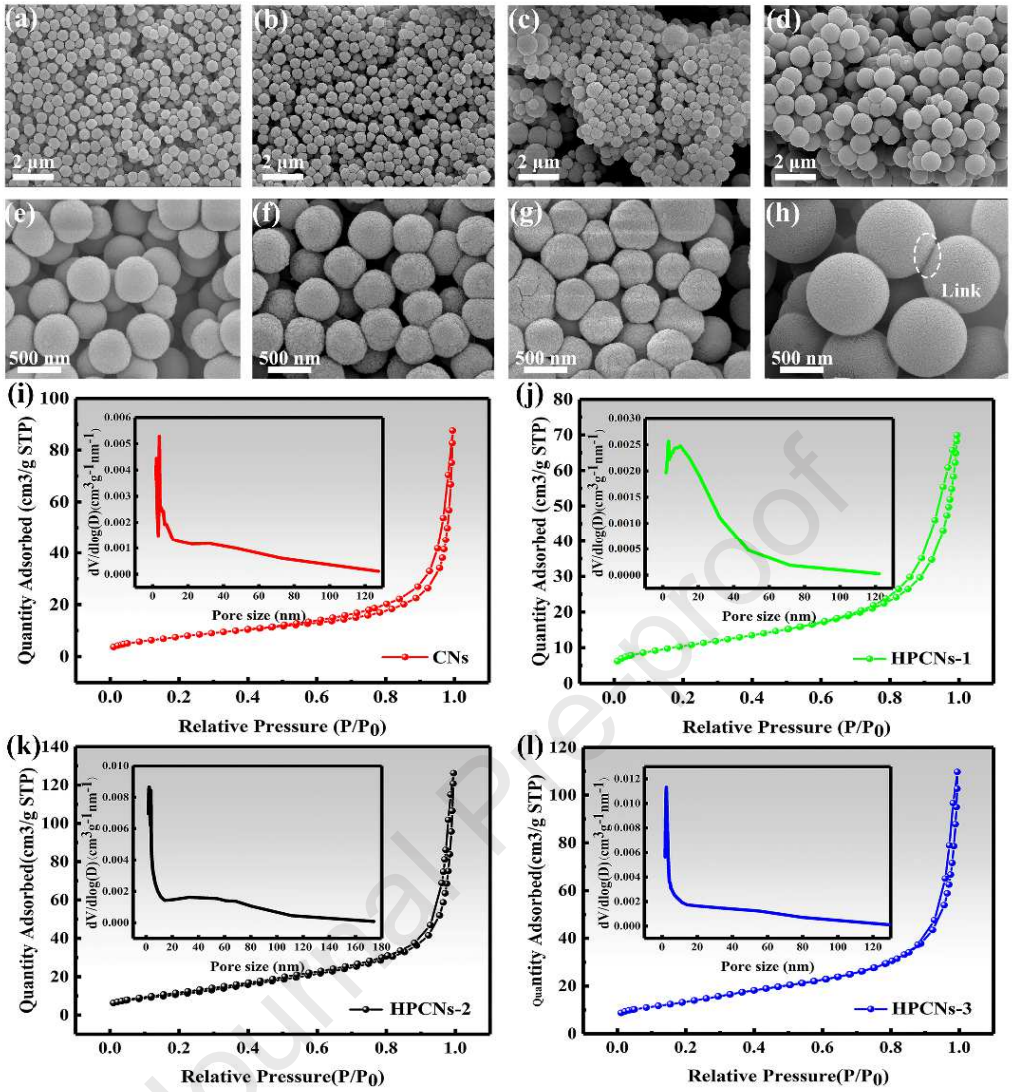

Fig. 2. SEM images of CNs (a, e), HPCNs-1 (b, f), HPCNs-2 (c, g), HPCNs-3 (d, h). Nitrogen adsorption-desorption isotherms and pore size distributions calculated result (i-l).

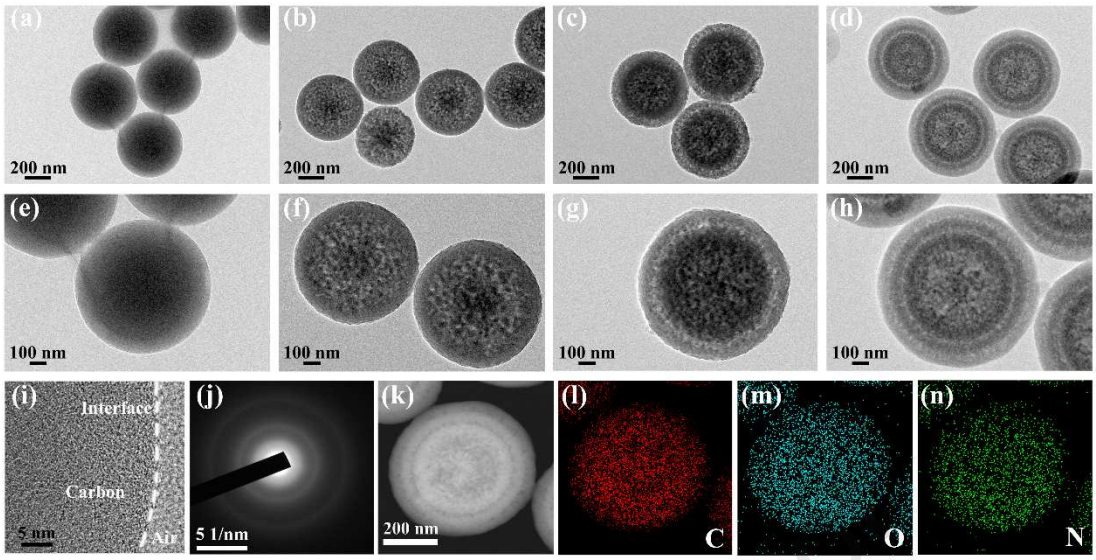

Fig.3. TEM images of CNs (a, e), HPCNs-1 (b, f), HPCNs-2 (c, g), HPCNs-3 (d, h). HR-TEM image (i)，SAED result (j) and Element mapping (k-n) of HPCNs-3.

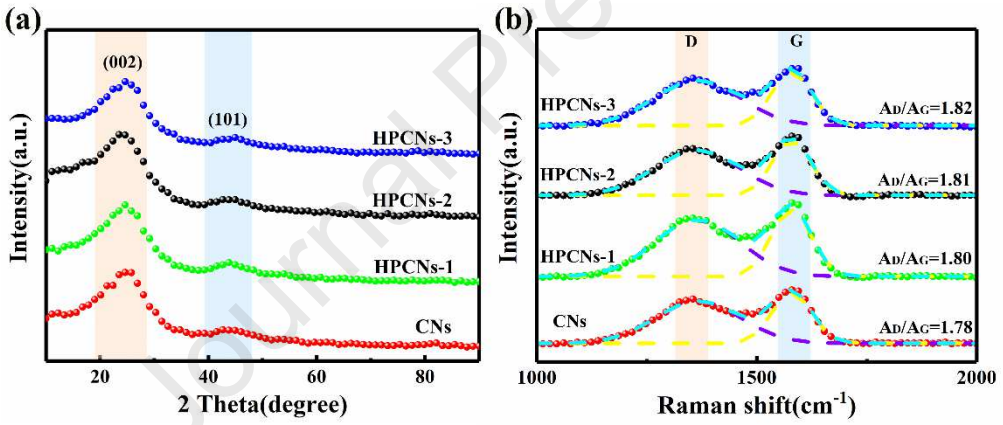

Fig. 4. XRD patterns (a) and Raman spectra (b) of samples.

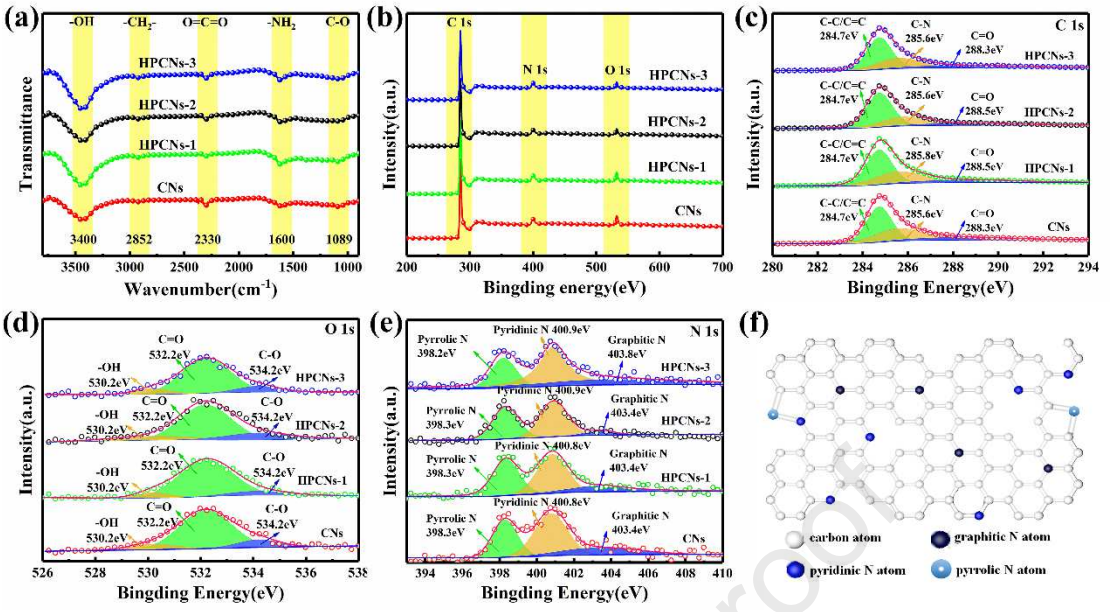

Fig. 5. FT-IR spectrum (a) and XPS spectrum (b) of samples, high resolution C 1s XPS spectrum of samples (c), high resolution N 1s XPS spectrum of samples (d), high resolution O 1s XPS spectrum of samples (e), schematic structure of N (f).

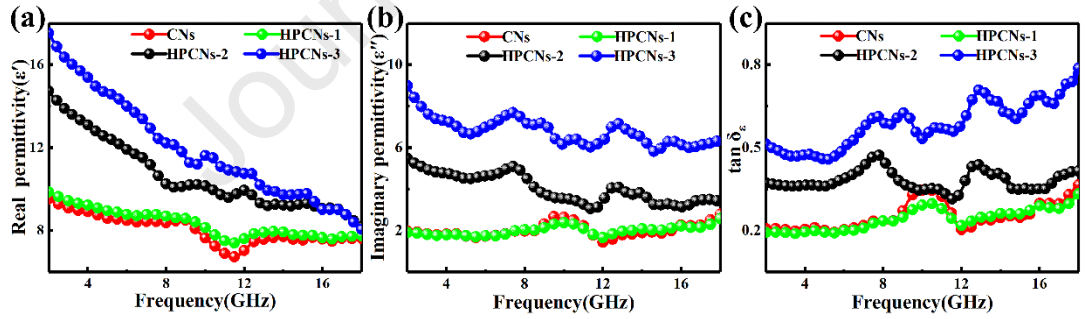

Fig. 6. The real (ε′) and imaginary (ε″) of complex permittivity (a, b), and tan δ_ε (c) versus frequency.

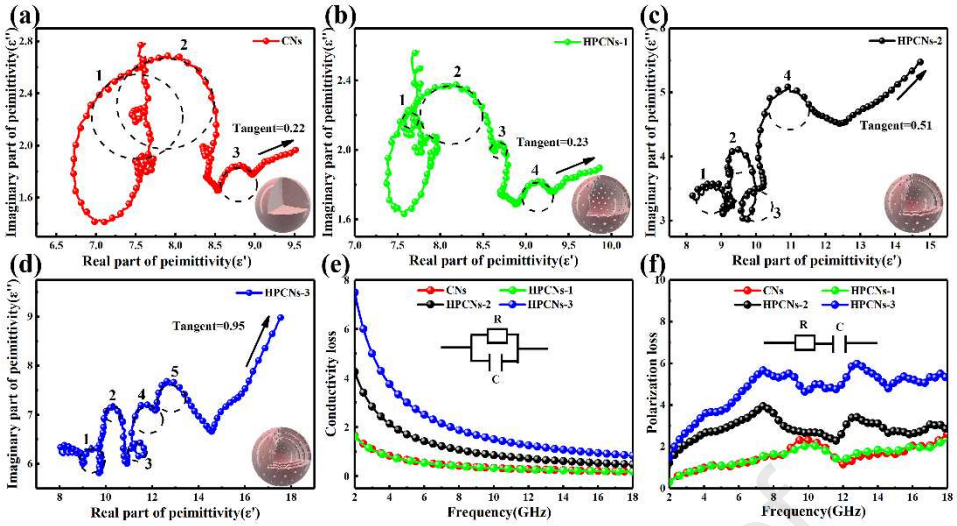

Fig. 7. Cole-Cole semicircles of CNs (a), HPCNs-1 (b), HPCNs-2 (c), and HPCNs-3 (d). Conductivity loss (e) and Polarization loss curve (f).

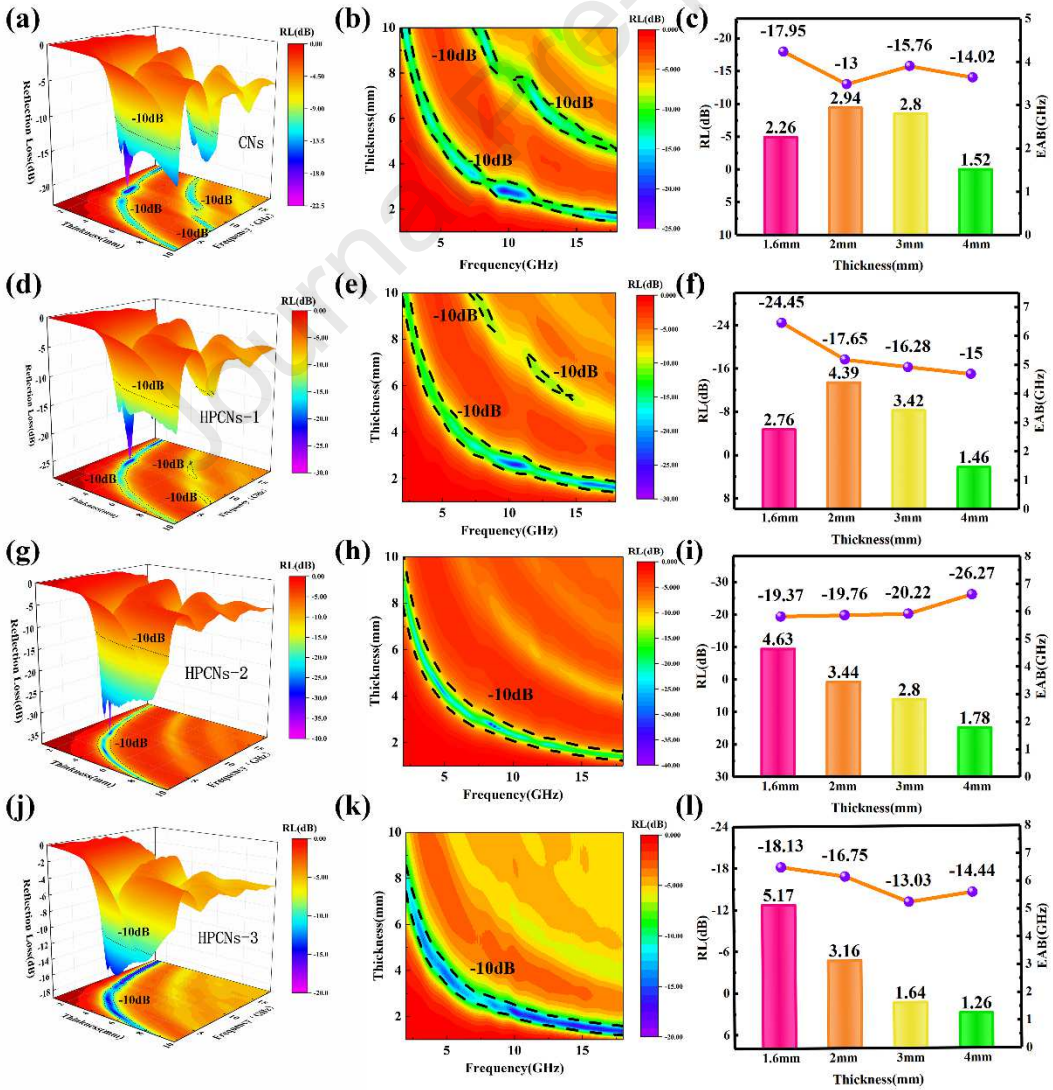

Fig. 8. 3D RL map, 2D RL contour map, RL value and EAB value between thickness range of 1.6–4.0 mm of CNs (a, b, c), HPCNs-1 (d, e, f), HPCNs-2 (g, h, i) and HPCNs-3 (j, k, l).

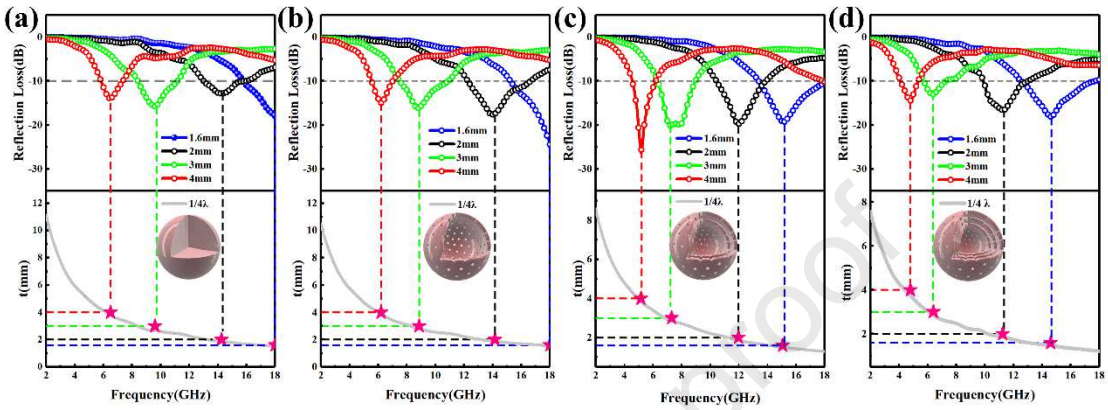

Fig. 9. Reflection loss (RL)-frequency curves, relationship between simulated thickness and the peak frequency for CNs(a), HPCNs-1(b), HPCNs-2(c), HPCNs-3(d).

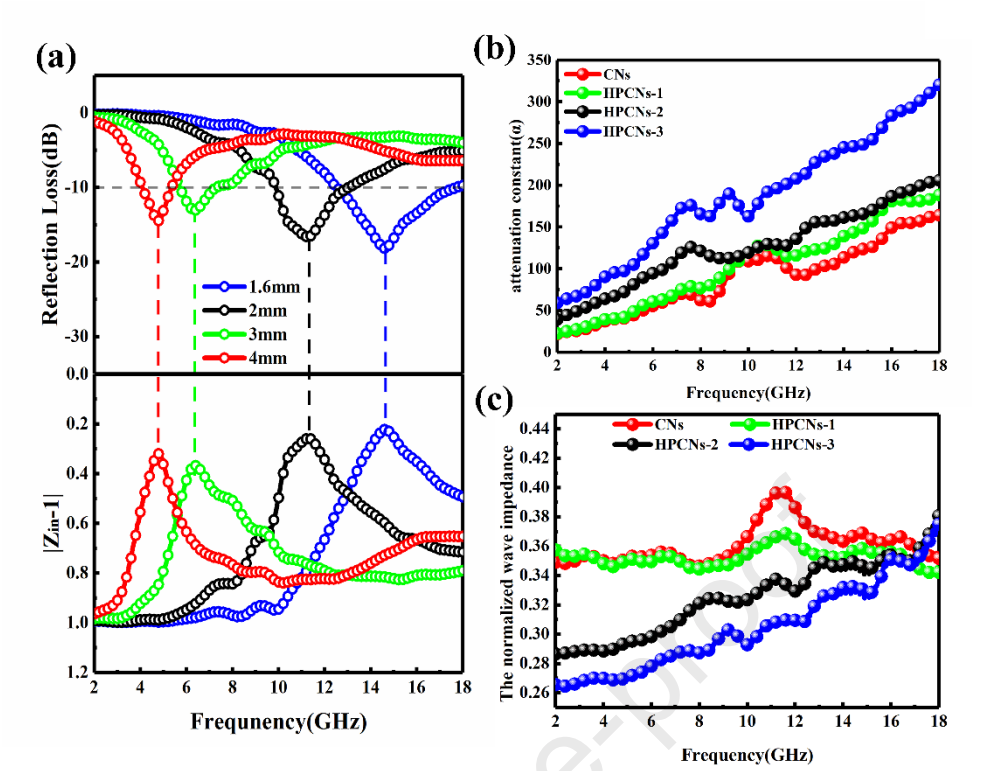

Fig. 10. The calculated $|Z_{in}-1|$ values represent for the impendence matching of HPCNs-3 (a). the normalized wave impedance (b) and attenuation constant (c) of all samples.

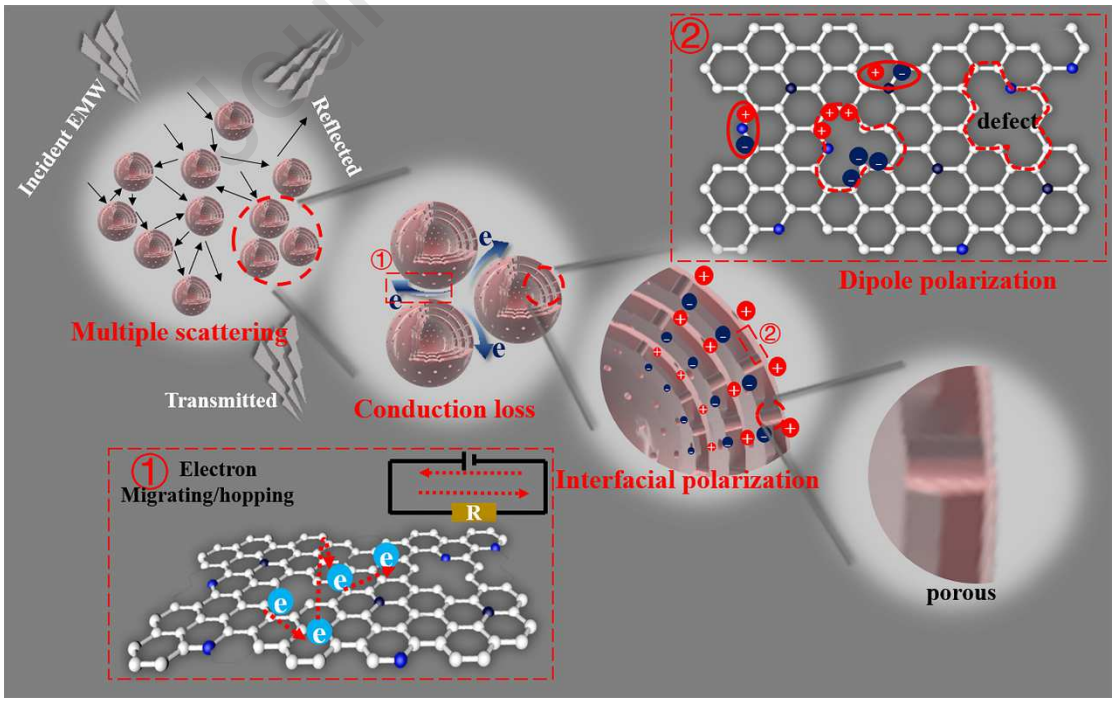

Fig.11. Schematic diagram of the microwave absorption mechanism of the

sample.

Highlights

1. The layer-by-layer process is used to prepare multi-shell hollow porous carbon nanoparticles with a complex structure

2. The multi-shell structure can significantly enhance the material's attenuation ability to electromagnetic waves

3. Three-shell hollow porous carbon nanoparticles can obtain an effective absorption bandwidth of 5.17 GHz at a thickness of 1.6 mm

Declaration of interests

☒ The authors declare that they have no known competing financial interests or personal relationships that could have appeared to influence the work reported in this paper.

☐The authors declare the following financial interests/personal relationships which may be considered as potential competing interests:

CRediT authorship contribution statement

Author contributions:

Jiaqi Tao: Conceptualization, Methodology, Writing-original draft, Investigation, Visualization, Project administration.

Jintang Zhou: Resources, Writing-review & editing, Supervision, Funding acquisition.

Zhengjun Yao: Formal analysis, Writing-Original Draft.

Zibao Jiao: Investigation, Visualization.

Bo Wei: Validation, Formal analysis, Investigation.

Ruiyang Tan: Validation, Formal analysis, Investigation.

Zhong Li: Writing-review& editing, Funding acquisition.